

# Effect of Prior Athermal Martensite on the Bainite Transformation Kinetics for a Medium Carbon Steel

Master Thesis

(August 2017)

By,

**Balaji Rengaraj Kamalraj**

to obtain the degree of Master of Science in Material Science and Engineering  
at Delft University of Technology, The Netherlands.

(balaji.kamalraj@gmail.com)

Supervised by,

Dr. Maria J. Santofimia  
Dr. Carola Celada- Casero  
Alfonso Navarro López



# Acknowledgements

I would like to express my sincere gratitude to my daily supervisor Dr. Carola Celada-Casero for helping me throughout my thesis and for being patient. The discussions and the knowledge transfer we had during the meetings helped me to improve with my thesis every day. I would also like to acknowledge Dr. Maria J. Santafoimia for the constant guidance during the discussion sessions and for sharing different ways to approach a problem. Her advice when I encountered a problem was exemplary. It would not be fair if I do not thank our Ph. D candidate Alfonso Navarro López for paving a path for the current thesis and having shared his work with me in the present study.

The help from Sander van Asperen, Richard Huizinga and Nico Geerlofs during my experiments were so timely, and I would like to extend my gratitude to every one of them. Even small discussions with Ph. D candidates Ashwath and Sudhindra were so helpful and valuable, and I had a great time talking to them. Thank you, both. I would also like to thank everyone who helped me throughout my thesis.

Last but not the least, I would like to thank my family (Dr. R. Kamalraj, Dr. D. Sasikala and Er. K. Cindhuja Renganayagi) and my friends who gave me the moral support and strength to finish my thesis successfully. I would also like to thank my friend Vitesh Shah for helping me with SEM and Thamizharasi Rasarasan for proof reading my report. I would like to dedicate this thesis to my niece, Riya Saanvika.





# Abstract

Bainitic steels have a right combination of strength and toughness when compared to that of martensitic and pearlitic steels. For the same reason, it is becoming a popular kind of steel among the automobile industry. It is important to study the bainite transformations to have an explicit knowledge about the same and to design bainitic steels accordingly based on the application which has to be satisfied. This requirement has led to an immense research on the bainitic steels in the recent past. One of the aspects which is studied recently is the behaviour of the transformation kinetics of bainite during the isothermal treatments. Factors like, austenite grain size, chemical composition (Si, Mn and C) and the presence of prior athermal martensite have been found to affect the transformation kinetics of bainite. The presence of prior athermal martensite (PM) has been reported to have an accelerating effect on the transformation kinetics of bainite by few of the authors. The two reasons given for the acceleration by two different school of thoughts are: 1.) due to the creation of additional potential nucleation sites from the martensite-austenite ( $\alpha'$ - $\gamma$ ) interfaces with the presence of prior athermal martensite (PM) and 2.) due to the strain induced (through dislocations) in the austenite matrix with the presence of PM. Therefore, further investigations are required to concrete the mechanism responsible for the acceleration. On the other hand, carbon content has been reported to have a decelerating effect on the kinetics of bainite formation due to the reduction in the driving force (based on the thermal stability of austenite). Thus, the effect due to the presence of PM and the effect due to the carbon content have opposite influence on the kinetics. It is important to study the effect of PM on the bainite transformation kinetics for steels with different compositions in order to understand if the alloying elements also have an effect on the kinetics. Having said that the carbon content has an effect on the kinetics, it will be interesting to study the effect of carbon content on the kinetics along with the presence of PM.

The primary goal of the current research is to examine the effect of prior athermal martensite (PM) on the kinetics of bainite transformation in a medium carbon steel (0.57 wt% C). In order to investigate the effect of carbon content, the current study will be compared with the research by A. Navarro-López et al. <sup>1</sup> which was on a low carbon steel (0.2 wt% C). There is clear evidence from the results of the current study that there is a competition between the decelerating effect of carbon content and the accelerating effect of PM at the beginning of the isothermal transformation. The results show that the carbon content has a significant role on the intensity of the acceleration effect due to the presence of prior athermal martensite.

**Keywords:** prior athermal martensite, bainitic ferrite, austenite decomposition, isothermal treatments, bainite transformation kinetics.

# Nomenclature

---

A	Area	$m^2$
V	Volume	$m^3$
$\Delta L$	Length change	m
$L_0$	Original length	m
$M_S$	Martensite start temperature	$^{\circ}C$
$B_S$	Bainite start temperature	$^{\circ}C$
$A_{C1}$	Austenization start temperature	$^{\circ}C$
$A_{C3}$	Austenization finish temperature	$^{\circ}C$
RT	Room temperature	$^{\circ}C$
G	Gibbs free energy	$J\ mol^{-1}$
f	Phase fraction	-
$\alpha$	Phase: ferrite	-
$\alpha'$	Phase: martensite	-
$\gamma$	Phase: austenite	-
BF	Bainitic Ferrite	-
LB	Lower Bainite	-
RA	Retained Austenite	-
MA	Martensite Austenite island	-
PM	Prior athermal Martensite	-
TM	Tempered Martensite	-
$B_{\alpha}$	Thermal expansion coefficient of ferrite	$K^{-1}$
$B_{\gamma}$	Thermal expansion coefficient of austenite	$K^{-1}$
$\theta_D$	Debye temperature	K
$\lambda$	Wavelength	m
HV	Hardness Vickers	HV

---

# Contents

<b>1. Introduction.....</b>	<b>1</b>
1.1. Overview.....	1
1.2. Introduction to AHSS.....	1
1.3. Phase Transformations.....	2
1.3.1. Martensitic Transformation.....	3
1.3.2. Bainitic Transformation.....	5
1.4. Bainite formation below $M_S$ .....	7
1.5. Kinetics of Bainite formation.....	8
1.5.1. Effect of Si, Mn and C.....	8
1.5.2. Effect of Prior athermal Martensite.....	8
1.6. Characterization of Bainite and Martensite formed below $M_S$ .....	10
1.7. Objective and Scope of the Thesis.....	12
<b>2. Experimental Methods.....</b>	<b>14</b>
2.1. Overview.....	14
2.2. Material.....	14
2.3. Heat treatments.....	16
2.4. Dilatometry.....	17
2.4.1. Equipment.....	17
2.4.2. Thermal expansion.....	18
2.4.3. Quantification of phase fractions.....	19
2.4.4. ‘Zero’ point for Bainite transformation.....	20
2.5. Metallographic preparation.....	21
2.6. X-ray Diffraction (XRD).....	22
2.7. Optical Microscopy.....	24
2.8. Scanning Electron Microscopy (SEM) and Energy Dispersive X-ray Spectroscopy (EDS).....	25
2.9. Micro-hardness Vickers measurements.....	25
<b>3. Results and Discussion.....</b>	<b>27</b>
3.1. Overview.....	27
3.2. Dilatation Analysis of Phases.....	27
3.2.1. Characterization of Martensitic Transformation.....	27
3.2.2. Identification of Phases from the Dilatation Data.....	28
3.3. Quantification of Phases.....	30
3.3.1. Volume Fraction of Retained Austenite (RA) from XRD.....	30
3.3.2. Volume fraction of Fresh Martensite (FM) and Prior Athermal Martensite (PM) from Dilatometry.....	32
3.3.3. Summary of the Phase Fractions.....	33
3.4. Microstructural Characterization.....	35
3.5. Micro-hardness Vickers measurements.....	39
3.6. Bainite Transformation Kinetics.....	40
3.6.1. Analysis with bainite transformation curves.....	40
3.6.2. Analysis with nucleation rate.....	43

3.6.3. Analysis based on the $n_{sites}$ .....	48
3.6.4. Effect of $\alpha'$ - $\gamma$ interfacial area .....	49
3.7. Effect of Carbon Content on the Transformation Kinetics of Bainite along with the presence of Prior athermal Martensite .....	50
<b>4. Conclusions</b> .....	<b>54</b>
<b>5. Recommendations</b> .....	<b>55</b>
<b>6. References</b> .....	<b>56</b>
<b>7. Appendix</b> .....	<b>a</b>
7.1. XRD calculation for all conditions .....	a
7.2. Phase Fractions with Corresponding Errors .....	j
7.3. Vacuum Effect at the Start of the Isothermal Transformation .....	k

# 1. Introduction

## 1.1. Overview

This chapter will begin explaining the importance of advance high strength steels (AHSS) along with the detailed description of phase transformations of martensite and bainite. Following this, the evidence for the formation of bainite below  $M_S$  and the kinetics of bainite formation based on several factors will be discussed based on the literature available. The characterization of bainite and martensite formed in the isothermal treatments below  $M_S$  will also be presented from the literature. The chapter ends with the objectives of the current thesis derived from the literature discussed in the current section.

## 1.2. Introduction to AHSS

Steels could be considered as one of the most popular materials because of its wide area of applications and low cost. One of the important factors to be considered while designing a steel is its mechanical properties (choice of mechanical properties depends on the application) which depends upon the microstructure of the steel. The microstructures can be controlled by varying the chemical composition and processing route. Various parameters during the processing route such as heating rate, cooling rate, austenization temperature/time and isothermal temperature/time decide the type of phase which is formed. Each phase has its own microstructural characteristics leading to its unique mechanical behaviour. Hence, the phase transformations play a significant role in the control of mechanical properties of steels.

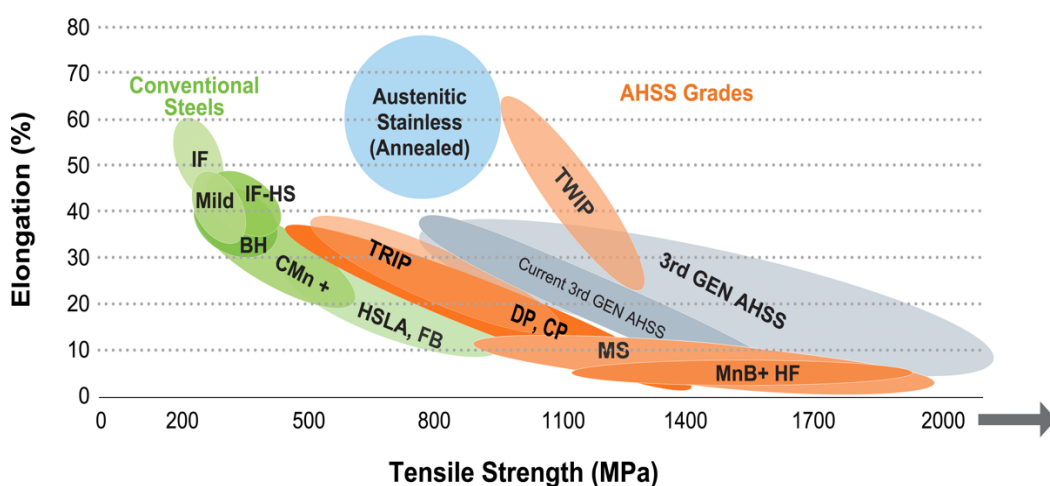


Figure 1.1: Evolution of steels as a function of strength and ductility. (Source: World auto steel)

AHSS is a prevalent family of steel among the automotive industry which is known for its excellent combination of strength (for performance) and ductility (for production). AHSS are evolving continuously to compete with conventional mild steels concerning ductility without

losing its strength, which will create a better balance between strength and ductility (see 3<sup>rd</sup> generation of AHSS in Figure 1.1). AHSS usually consist of a complex multi phase microstructures with carefully selected chemical composition and precisely controlled heating and cooling processes. The family of AHSS includes dual phase (DP), complex-phase (CP), ferritic-bainitic (FB), martensitic (MS), transformation-induced plasticity (TRIP), hot-formed (HF), and twinning-induced plasticity (TWIP) steels as shown in Figure 1.1.

The phase transformations (martensitic and bainitic transformations in particular) play a vital role in the development of AHSS. The reason for considering martensitic and bainitic transformations important is because they contribute for the majority of the strength when compared to other phases such as ferrite, pearlite and austenite. For instance, martensitic formation from fully austenite microstructure involves transformation from face centred cubic to body centred tetragonal structure (supersaturated with carbon) resulting in a large increase in the volume. This increase in the volume results in a highly stressed structure. The shear deformation involved during the transformation produces a large number of dislocations which is the primary strengthening mechanism of steels. Apart from phase transformations, there are also other mechanisms such as solid solution strengthening, grain refinement, work hardening and precipitation hardening which lead to strengthening. Having said that the development of 3<sup>rd</sup> generation AHSS with an improved combination of strength and ductility is in progress, it is important to consider a combination of phases like martensite and bainite. Based on the fact that the phase transformations are important in the development of AHSS, the phase transformation of martensite and bainite will be discussed in the following sections.

### 1.3. Phase Transformations

During heating, cooling, isothermal treatments and plastic deformation of the steel for a given composition, phase transformations occur based on the condition which is applied. For instance, when cooling takes place from the austenization temperature, austenite transforms into various phases such as ferrite, pearlite, bainite and martensite. The resulting phase from the decomposition of austenite depends on the heating rate to reach austenization and the cooling rate from the austenization temperature<sup>2</sup>. The factors influencing the microstructure formed during cooling are the chemical composition of the steel together with the cooling rate and the prior thermal history. The microstructure of the steel formed during cooling determines the mechanical properties such as strength and toughness. Understanding the phase transformations involved is therefore of primary importance to optimise the resulting mechanical properties.

Any phase transformation in the solid state involves nucleation and growth. Based on the mechanism by which the new phase is formed, two kinds of phase transformations can be distinguished: reconstructive and displacive transformations. The characteristics of the diffusion controlled transformations from austenite to ferrite and pearlite are given in the references<sup>2-4</sup>. But there is still a controversy over the transformation mechanism of the bainite where one school of thought says that the transformation is displacive and the other school argues that the transformation is diffusional based<sup>5-9</sup>. Though the microstructure in the current

study will have a mixture of martensite, bainite and retained austenite, the transformation and kinetics of the martensite and bainite will be the key area of study in this research. Thus the martensitic and bainitic transformations will be discussed in detail in the following sections.

### 1.3.1. Martensitic Transformation

Martensite is a phase which is formed in carbon steels during a rapid quench of austenite form of iron where not enough time is provided to the carbon atoms to diffuse out of the crystal structure in large quantities to form cementite. As a result of this, a highly strained body centred tetragonal (BCT) structure that is supersaturated with carbon is formed from the austenite which is face centred cubic (FCC).

The martensitic transformation is a diffusionless and displacive first-order transformation during which the lattice distortion can be described by a combination of shears<sup>10</sup>. It involves a simultaneous and cooperative movement of atoms from parent to product phase. This type of phase transformation is also called a displacive or shear transformation.

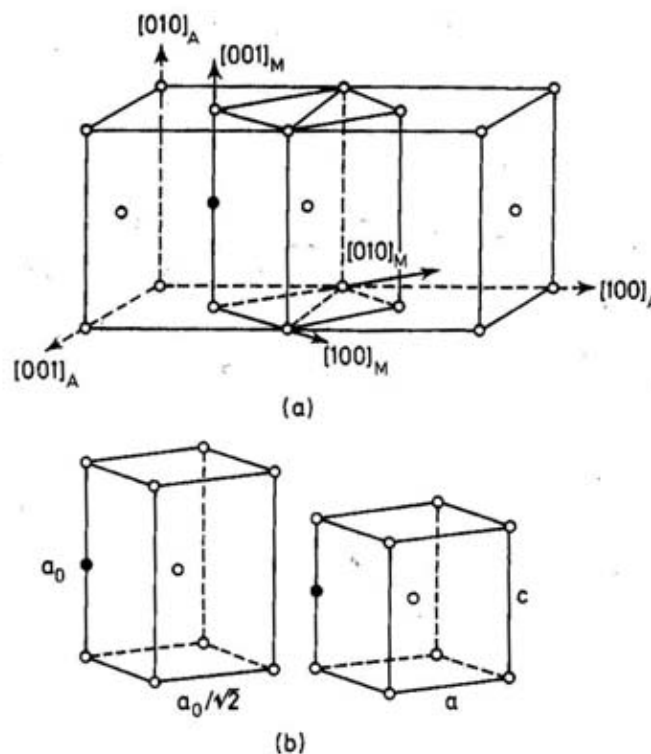


Figure 1.2: The Bain correspondence. (a) Two FCC austenite cells to show that a tetragonal cell can be outlined in austenite (b) Bain strain of this cell with axial ratio  $\sqrt{2}$  into BCT martensite with  $c/a$  ratio depending on the carbon content<sup>3</sup>

Due to the displacive character of the transformation, the composition of the martensite replicates its parent austenite. Since the martensitic transformations are rapid, there is only limited time for the carbon atoms to diffuse and consequently, the carbon atoms are trapped in the octahedral sites of the body centred cubic (BCC) lattice structure. In such cases, the amount

of carbon exceeds the solubility in ferrite, and hence the martensitic phase in steel can be simply described as a super-saturated solution of carbon in the ferrite phase, in which the excess carbon content leads to the tetragonal structure of the lattice. The correspondence in the lattice structure between the austenite and martensite was first discovered by Bain. It was shown that a body centred tetragonal (BCT) unit cell could be constructed between two face centred cubic (FCC) unit cells as shown in the Figure 1.2a. The strain which is necessary to transform this BCT unit cell into a martensite unit cell is known as the Bain strain. This strain has a contraction along the  $z$ -axis and uniform expansion along the  $x$  &  $y$ -axis (Figure 1.2b). The tetragonality of the BCT structure increases with increasing carbon concentration as shown in Figure 1.3<sup>11</sup>.

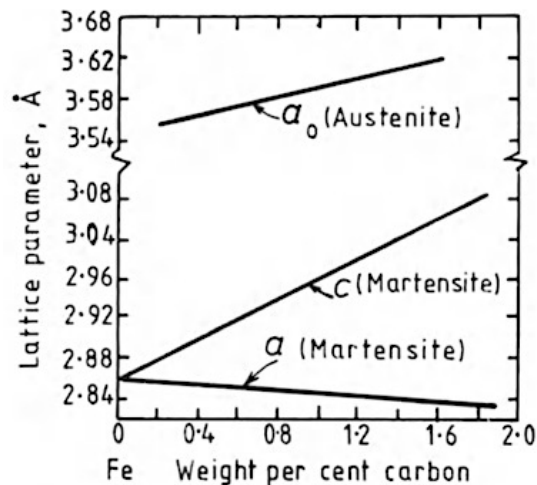


Figure 1.3: Variation of  $a$  and  $c$  in BCT lattice as a function of carbon content<sup>11</sup>.

Owing to the high carbon content (due to faster cooling rate), the martensitic crystal structure (BCT) is a metastable phase. In case the temperature is increased, the carbon atoms become mobile and will diffuse from the martensite lattice to form carbides. This phenomenon can be called as tempering process. During this process, the martensite decomposes into a mixture of ferrite and cementite, with concentrations according to the Fe-C phase diagram. Precipitation of carbides inside the martensite lath is also observed during the tempering process which reduces the supersaturation of carbon in the as-quenched martensite after the tempering process<sup>12</sup>.

The transformation from austenite to martensite is referred to as athermal since the transformation occurs due to the decrease in temperature and not as a function of time. The free energy of the martensite ( $\alpha'$ ) has to be lesser than that of the austenite ( $\gamma$ ) for the transformation to occur. Martensitic transformations start at a temperature lower than the  $T_0$  (temperature at which free energies of austenite and martensite are the same) since the additional energy in the form of surface energy and strain energy is required for the transformation to start, and that temperature is called as the martensite start temperature ( $M_S$ ). The driving force for the transformation comes from the temperature difference between  $T_0$  and  $M_S$ <sup>10</sup>. The effect of the carbon content on the  $M_S$  temperature can be seen in Figure 1.4<sup>12</sup> and it is found that they are inversely proportional to each other. The decrease in the  $M_S$  temperature results in the increase in retained austenite volume fraction in an as-quenched microstructure. It can also be seen from the Figure 1.4 that the morphology of the martensite



depends on the carbon content where a lath morphology will be seen for the low carbon steels and a plate morphology for the high carbon steels.

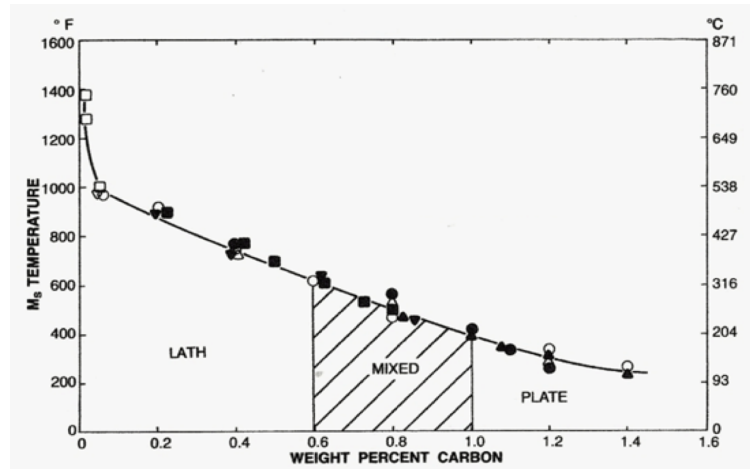


Figure 1.4: Effect of carbon content on the  $M_s$  temperature and the morphology of the martensite <sup>12</sup>.

### 1.3.2. Bainitic Transformation

As mentioned earlier, reconstructive model and displacive model are the two different models which have been proposed by two schools of knowledge to describe the transformation kinetics of bainite <sup>7-9</sup>. The reconstructive model for the bainite transformation assumes that the transformation takes place through the diffusion of atoms. This means that the formation of ferrite and cementite from the austenite is assisted by diffusional processes <sup>8</sup>. This mechanism is similar to that of the formation of pearlite, but the typical lamellar structure seen in the pearlite does not occur here.

The assumption made in the displacive model is that the substitutional atoms rearrange during the bainite formation in a diffusionless fashion <sup>7,9</sup>. There is also another assumption that the creation of sheaves of bainite follows the mechanism of martensite formation which is diffusionless and is followed by the rejection of excess carbon into the remaining austenite which subsequently leads to the formation of carbides. The precipitation of cementite can be retarded by the addition of Si since Si is insoluble in cementite <sup>7,13</sup>. In this model, even though the growth occurs without diffusion, the nucleation at the austenite grain boundaries still require some partitioning of carbon <sup>9,14</sup>.

The microstructural appearance of bainite differs considerably due to certain changes during and/or after the phase transformation. Bainite can be defined as an aggregate of ferrite plates separated by residual phases such as untransformed austenite and cementite. The individual plates of ferrite are usually called as subunits, and a group of such subunits are called as sheaves. As the transformation temperature decreases, the size of the bainite subunits decreases and thus the density of ferrite plates increases with the decrease in transformation temperature <sup>15</sup>.

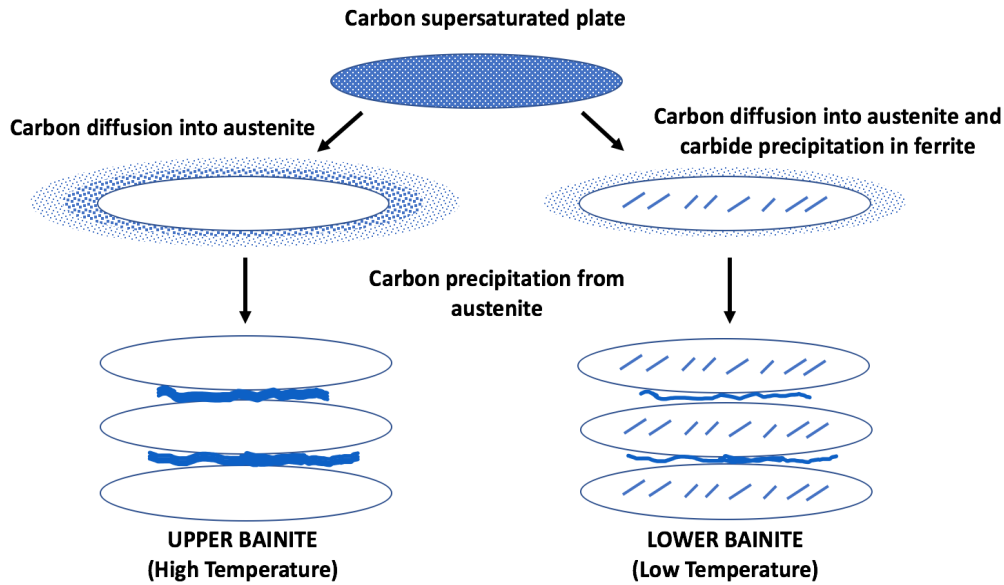


Figure 1.5: An illustration of the growth of bainite and the development of upper or lower bainite <sup>16</sup>.

Regarding the morphology of bainite, two primary structures can be identified which are called upper and lower bainite as shown in Figure 1.5. Upper bainite forms at a relatively high temperature, usually in the range of 600-450 °C and lower bainite between 450 °C and  $M_S$  temperature (Figure 1.6) <sup>17</sup>. The morphology of lower bainite and upper bainite are distinct from one another. In the case of upper bainite, there will be no carbides precipitated inside the ferrite plates and the precipitation of cementite is seen only in the interlath austenite between the ferrite plates which is enriched in carbon. Whereas in the case of lower bainite, the carbon content in the bainitic ferrite is higher due to the low diffusivity of carbon at low temperatures and this leads to the carbide precipitation inside the plates of bainitic ferrite. The carbides inside a single ferrite plate of lower bainite usually are aligned along the same axis parallel to each other. Therefore, two types of cementite can be recognised in lower bainite: cementite particles that precipitated from the carbon enriched austenite and cementite particles that precipitated from supersaturated ferrite. The latter precipitation shows a strong resemblance with the tempering of martensite. The layers of carbide in lower bainite are usually extremely fine compared with those in upper bainite. Consequently, steels with lower bainitic microstructure are tougher than the steels with upper bainitic microstructure. Moreover, lower bainite is stronger than upper bainite since the precipitates are finer.

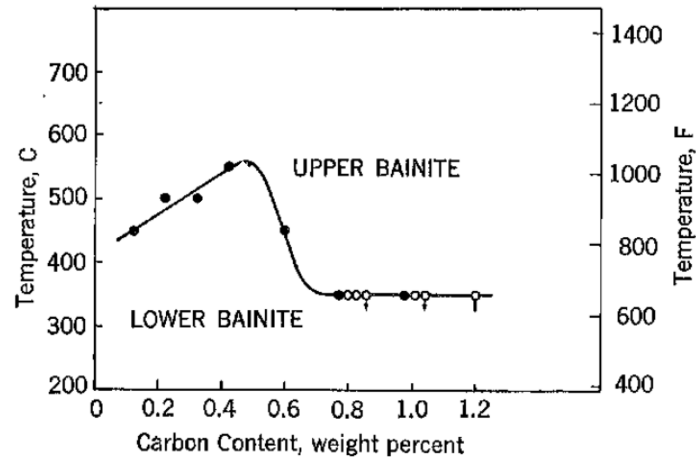


Figure 1.6: Effect of carbon content on the transition temperature from upper to lower bainite, the line indicates the temperature above which lower bainite was never observed<sup>17</sup>.

The number of cementite particles in bainite does not only depend on the carbon concentration but also on the alloying elements. For example, by increasing the silicon concentration to retard the cementite precipitation as mentioned earlier.

#### 1.4. Bainite formation below $M_S$

The possibility of formation of bainite below  $M_S$  has been studied by a few researchers. The bainite transformation below the  $M_S$  was confirmed by van Bohemen et al.<sup>18</sup> and Kolmskog et al.<sup>19</sup> for the medium carbon steels (0.5-0.65 wt% C). In the paper of van Bohemen et al.<sup>18</sup>, the magnitude of time dependent dilatation below and above  $M_S$  temperature were compared and found to be in line with each other. More evidence such as the characterization of the microstructures through SEM micrographs and comparison of thermal expansion values were provided. All this put together showed that the transformation product below  $M_S$  was bainite. The research by Kolmskog et al.<sup>19</sup> provided evidence using an in-situ simultaneous synchrotron X-ray diffraction and laser scanning confocal microscopy where the synchrotron data clearly showed the evolution of BCC{110} and FCC{111} peaks during the start of the isothermal treatment below  $M_S$  which proved the formation of bainite during the isothermal treatment.

The research by Kim et al.<sup>20-22</sup> for a low carbon steel (0.2 wt% C) described that the isothermal product below the  $M_S$  looked much thicker than the prior athermal martensite lath with wavy boundary and ledges along the boundaries. The isothermal product also had multivariant carbides in it which is a character of prior athermal martensite after tempering. But the author described the nature of the isothermal product as neither bainitic nor martensitic. Research by A. Navarro-López et al.<sup>1,23</sup> for a low carbon steel (0.2 wt% C) described that the isothermal product formed below the  $M_S$  was bainitic based on the microstructural characterization by SEM and EBSD analysis. Hence there is still a small uncertainty with the kind of isothermal product formed below the  $M_S$  temperature.

## 1.5. Kinetics of Bainite formation

One of the important aspects of the bainite transformation is the kinetics involved. The study of the kinetics of bainite during the isothermal treatment is very important in terms of knowledge and efficiency during the production process. There have been a lot of studies on the bainite transformation kinetics based on factors like austenite grain size, chemical composition (C, Si, Mn) and the presence of prior athermal martensite (PM), and they will be discussed in detail in the upcoming sub-sections.

### 1.5.1. Effect of Si, Mn and C

The effect of the Si, Mn and C content on the kinetics of bainite formation during the isothermal treatments have been reported by few authors. T. Sourmail et al.<sup>24</sup> and Y. Toji et al.<sup>25</sup> (both for high carbon steels: 0.8-1 wt% C) have reported that the Si content has a continuous retarding influence on the bainite transformation kinetics. The reason for this was mentioned to be the enhanced carbon partitioning (due to retardation of carbide precipitation due to high Si content) into the austenite, substantially stabilising the austenite and leading to the retardation of subsequent bainite transformation<sup>26,27</sup>. But a contrasting result by Karbakhsh Ravari et al.<sup>28</sup> for a hyper eutectoid steel (0.7 wt% C) described that the Si has an accelerating effect on the transformation kinetics of bainite.

The effect of Mn on the kinetics has also been reported by Karbakhsh Ravari et al.<sup>28</sup> and was found to have a decelerating effect on the transformation kinetics of bainite during the isothermal treatments.

The effect of the carbon content on the kinetics of bainite formation was studied by Kangying Zhu et al.<sup>27</sup> for two different carbon contents. It was found that the increase in C content from 0.155 to 0.319 wt% retards the bainite transformation kinetics considerably at all the isothermal temperatures (550 °C, 500 °C and 430 °C) which were studied. Regarding the effect of carbon content on the bainitic and martensitic transformations, it is well accepted that an increase in carbon content retards both martensite and bainite formation since it decreases the driving force for the transformations<sup>29-31</sup>.

### 1.5.2. Effect of Prior athermal Martensite

The thermomechanical processing of AHSS also incorporates isothermal treatments around the martensite start temperature ( $M_S$ ). A sudden acceleration in the kinetics of subsequent transformation has been observed when the isothermal treatment was done below  $M_S$  which could be related to the introduction of prior athermal martensite into the austenite matrix<sup>1,25,32-44</sup>. The approach which has been used in such studies included two sets of isothermal heat treatments: 1. Isothermal treatment above  $M_S$  (without prior martensite) and 2. Isothermal treatment below  $M_S$  (with prior martensite). This approach is shown in Figure 1.7 with two lines of heat treatment (1-2-4-5 and 1-3-4-5).

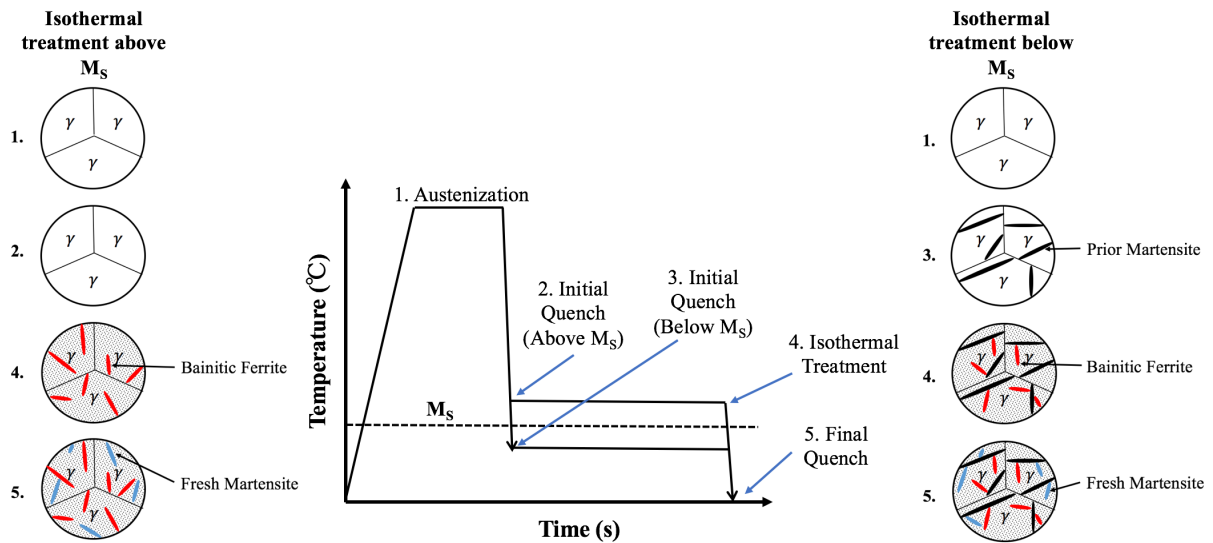


Figure 1.7: Schematic of the isothermal treatments above and below the  $M_S$  temperature and the subsequent phases formed. The steps 1, 2, 4, 5 is for the isothermal treatment above  $M_S$  temperature and the steps 1, 3, 4, 5 is for the isothermal treatment below the  $M_S$  temperature.

The effect of the prior athermal martensite on the transformation kinetics of bainite has been studied by quite a few authors recently. Researches from W. Gong et al.<sup>32</sup>, Smanio et al.<sup>33</sup>, Y. Toji et al.<sup>25</sup>, H. Kawata et al.<sup>34</sup>, E.P. Da Silva et al.<sup>35</sup>, Howard et al.<sup>41</sup>, Goodenow et al.<sup>39</sup> and A. Navarro-López et al.<sup>1</sup> have described that the presence of prior athermal martensite before the start of the isothermal treatment accelerates the kinetics of bainite transformation. The chemical composition of the steels studied was quite different from one another where the carbon content varies between 0.2-1 wt%. The results were derived by comparing the isothermal treatments above and below  $M_S$ .

The research by A. Navarro-López et al.<sup>1</sup> (0.2 wt% C) showed that the introduction of a very small fraction of prior athermal martensite (0.04) already accelerates the transformation kinetics at the start of the transformation quite predominantly (where the nucleation rate increased in the order of  $10^5$  in magnitude when compared to the condition above  $M_S$ ).

Another interesting effect was emphasized in the work of E.P. Da Silva et al.<sup>35</sup> (0.3 wt% C), where it was stated that the acceleration was predominant for the isothermal treatments just below  $M_S$  ( $\sim 10^\circ\text{C}$  below  $M_S$ ) but the acceleration dropped during the isothermal treatments well below  $M_S$  ( $\sim 90^\circ\text{C}$  below  $M_S$ ). Hence the author concluded that the bainite transformation kinetics below  $M_S$  depends on the temperature of the isothermal treatment and the volume fraction of PM. Thus it is quite clear from all these researchers that the acceleration effect is observed in the transformation kinetics of bainite with the presence of PM.

Having said that the presence of PM accelerates the bainite transformation kinetics, the mechanism involved in the acceleration could be argued between two concepts:

1. The presence of  $\alpha'$ - $\gamma$  interface serving additional potential nucleation sites for the transformation.
2. Strain induced (through dislocations) in the austenite with the presence of martensite.

Kawata et al.<sup>34</sup> and A. Navarro-López et al.<sup>1</sup> have reported in support of the first mechanism. In the research of Kawata et al.<sup>34</sup>, a comparison between the acceleration of bainite transformation induced by the presence of prior athermal martensite and prior ferrite (both in same fractions) was made. It has to be noted that the presence of prior athermal martensite (PM) introduces strain into the austenite matrix and whereas the presence of prior ferrite does not. It was found that the acceleration effect was similar for both conditions which mean that the effect due to the interfacial area between the austenite and prior martensite/ prior ferrite predominates over the effect due to the strain introduced into the austenite. A. Navarro-López et al.<sup>1</sup> have reported that the increase in the fraction of the PM increased the acceleration effect, but it was not proportional to each other. The reason for this was described as the interfacial area of the  $\alpha'$ - $\gamma$  interface is the key to the acceleration rather than the volume fraction of PM.

On the other hand, Howard et al.<sup>41</sup>, Goodenow et al.<sup>39</sup> and Y. Toji et al.<sup>25</sup> have reported in favour of the second mechanism. Howard et al.<sup>41</sup> have reported the formation of many bainite subunits away from the martensite plate which means that the interface of austenite-martensite does not affect the acceleration. Thus the acceleration was related to the strain introduced by the martensite plate on the austenite. In the research of Goodenow et al.<sup>39</sup>, the acceleration of the upper bainite was observed with the presence of prior lower bainite. But when the lower bainite was annealed (to release the strain) before the start of the isothermal transformation of upper bainite, the acceleration effect was not observed. This observation showed that the acceleration earlier was caused due to the strain introduced by the lower bainite on the austenite matrix. Y. Toji et al.<sup>25</sup> claimed that the acceleration is due to the dislocations introduced by the formation of PM in the austenite matrix. This claim was based on the arrangement of bainite units around the martensite plate for two different high carbon steels, one with Si (2.2 wt%) and one without Si. Thus the mechanism for the acceleration of the bainite transformation due to the presence of PM remains unclear and requires further studies to concrete the mechanism responsible for the acceleration.

## 1.6. Characterization of Bainite and Martensite formed below $M_S$

Research by A. Navarro-López et al.<sup>23</sup> characterizes the structural and morphological features of the product phases by SEM and EBSD obtained during the isothermal treatments above and below  $M_S$  temperature for a low-carbon high-silicon steel (0.2C-1.52Si wt%). The different structural features found in the microstructure and the phase to which it belongs for above and below  $M_S$  conditions are shown in Figure 1.8 and Table 1.1 respectively.



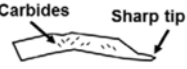


Structural Feature	Schematic Representation
$S_{Thin} (S_T)$	 Acicular units
$S_{Irregular} (S_I)$	 Irregular shape
$S_{Thick} (S_{TK})$	 Carbides Sharp tip
$S_{Elongated} (S_E)$	 Wavy Boundary Carbides
$S_{Blocky} (S_B)$ (MA island)	 Small laths RA

Figure 1.8: Schematic representations of the different features described, directly derived from actual micrographs<sup>23</sup>.

Table 1.1: Summary of the microstructural features observed in isothermal treatments at 340 °C, 320 °C, 300 °C and 270 °C. The nature and characteristics of each feature are also in detail<sup>23</sup>

Structural Feature	Characteristics	340°C	320°C	300°C	270°C	Phase Nature
$S_{Thin} (S_T)$	- Above and below $M_s$ . - Thin units with acicular shape. - Parallel aligned. - Length: 5-8 $\mu\text{m}$ . - No carbides distinguished.	✓	✓	✓	?	Bainitic
$S_{Irregular} (S_I)$	- Above and below $M_s$ . - Laths with irregular shape. - Wider than $S_T$ . - No carbides distinguished.	✓	✓	✓	---	Bainitic
$S_{Thick} (S_{TK})$	- Below $M_s$ . - Laths with sharp tip at an edge. - Surrounded by $S_T$ . - Contain carbides.	---	✓	✓	✓	Martensitic
$S_{Elongated} (S_E)$	- Below $M_s$ . - Longer and wider than $S_T$ . - Wavy boundaries. - Contain carbides.	---	✓	✓	✓	Martensitic
$S_{Blocky} (S_B)$ (MA island)	- Smooth surface (not etched). - Internal structure. - Very small laths. - Surrounded by RA blocks.	✓	✓	✓	✓	Martensite / Austenite

The microstructure obtained in the isothermal treatments above  $M_s$  had a mixture of thin ( $S_T$ ) and irregular structures ( $S_I$ ) with no carbides precipitated inside them. These two structures were identified as bainitic ferrite since there was no formation of athermal martensite before the start of the isothermal treatment. MA islands were also found in the conditions above  $M_s$ . EBSD showed that the MA islands had small martensite laths surrounded by small blocks of retained austenite.

In the isothermal treatments below  $M_s$ , the microstructure had a mixture of thin structures ( $S_T$ ), irregular structures ( $S_I$ ) and MA islands similar to that of the conditions above



$M_S$ . In addition to this, thick ( $S_{TK}$ ) and elongated structures ( $S_E$ ) which had multivariant carbides inside them were also found in the microstructure. These features could be related to the presence of athermal martensite before the start of the isothermal treatment since the isothermal treatments were below  $M_S$ . Since the thin ( $S_T$ ) and irregular structures ( $S_I$ ) found in conditions below  $M_S$  were similar to that of the conditions above  $M_S$ , they were assigned to be bainitic ferrite.

## 1.7. Objective and Scope of the Thesis

It is evident from the literature that the effect of PM on the transformation kinetics of bainite is not well understood. There are certain controversies on the mechanism of the acceleration effect which needs to be solved in order to understand the acceleration effect due to the presence of PM thoroughly. The effect of PM and carbon content on the transformation kinetics of the bainite formation has been studied separately by many authors. A study on the behaviour of the effect of PM with compositional variation could lead to a better understanding of the phenomenon and open up new possibilities for the future. Hence, the effect of PM on the transformation kinetics of bainite with varying carbon contents will be studied in the present research. In order to study the effect of PM on the transformation kinetics of bainite, a medium carbon steel of composition Fe-0.57C-2.11Mn-0.006Si (in wt%) has been used in the current research.

The key research question which will be addressed in the current study is:

- What is the effect of the prior athermal martensite (PM) on the transformation kinetics of bainite with varying carbon contents: low carbon (0.2 wt% C) and medium carbon steel (0.57 wt% C)?

In order to answer this research question, the study will be focused on:

- Comparison of the evolution of volume fraction of bainite as a function of time for conditions with and without PM.
- Comparison of the evolution of nucleation rate as a function of bainite volume fraction for conditions with and without PM.
- Comparison of the number of bainite nuclei formed per second in the austenite grain for conditions with and without PM.

A similar procedure (as given above) has been used in the research of A. Navarro-López et al. <sup>1</sup> to study the effect of PM on the bainite transformation kinetics for a low carbon steel (Fe-0.2C-3.51Mn-1.52Si-0.25Mo-0.04Al in wt%). In order to study the effect of the carbon content along with the effect of PM on the kinetics, the present study will be compared to the research of A. Navarro-López et al. <sup>1</sup>.



The report consists of different sections as follows: *Introduction (current section)*, explaining the available literature serving as the motivation for the current research, *Experimental procedure* illustrating the complete procedure in which the experiments were conducted, *Results and Discussion* portraying the results from the experiments and characterization along with a detailed discussion on the correlation of results obtained and finally the *Conclusion & Recommendations*, which will summarize the report and the results obtained along with a list of recommendations for the future research on a similar topic. The investigation in this current research was handled by dilatometry, XRD, EDS, optical microscopy, SEM and micro-hardness Vickers test.

# 2. Experimental Methods

## 2.1. Overview

This chapter will deal with the details on the experimental procedures done in this current study. The alloy used is introduced along with the selected theoretical properties of this alloy which are calculated alongside. An overview of the heat treatments performed in this work and the post-processing of the resulting samples is presented. Furthermore, the experimental details on the equipment used are also explained. Dilatometry, X-ray diffraction and hardness measurements are extensively treated whereas the scanning electron microscopy and optical microscopy are treated briefly assuming that the reader is familiar with these techniques.

## 2.2. Material

The material used in this study is a medium carbon manganese steel with lean amounts of silicon. The composition in weight percent is given in Table 2.1. After casting, the steel was hot rolled to a final thickness of 6 mm thickness and then air cooled to room temperature.

Table 2.1: Composition of the steel used in the current study (in wt %) with balanced Fe.

C wt%	Mn wt%	Si wt%	Mo wt%	Al wt%	N wt%	S wt%	P wt%	Cr wt%
0.57	2.11	0.006	<0.005	0.001	<0.001	<0.001	<0.002	<0.005

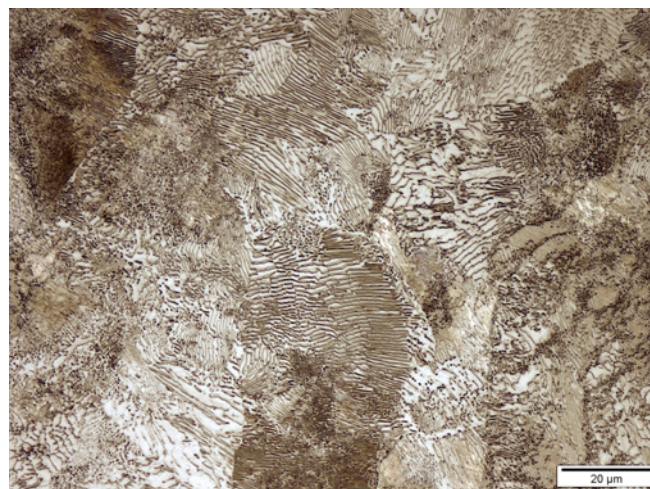


Figure 2.1: The initial microstructure (fully pearlitic) of the steel under investigation.

Figure 2.1 shows an optical micrograph portraying the initial microstructure of the steel under investigation. The microstructure is fully pearlitic (lamellar structure with alternating layers of ferrite and cementite).

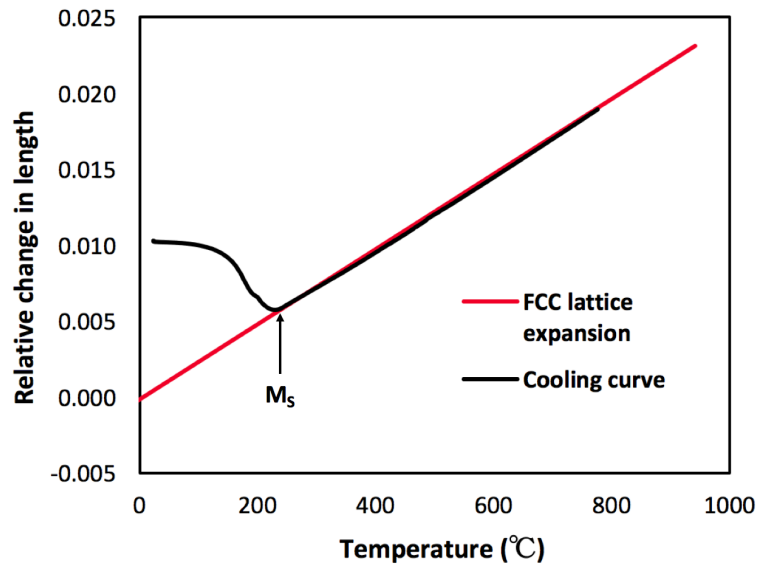


Figure 2.2: Determination of  $M_S$  temperature by linear extrapolation of FCC expansion.

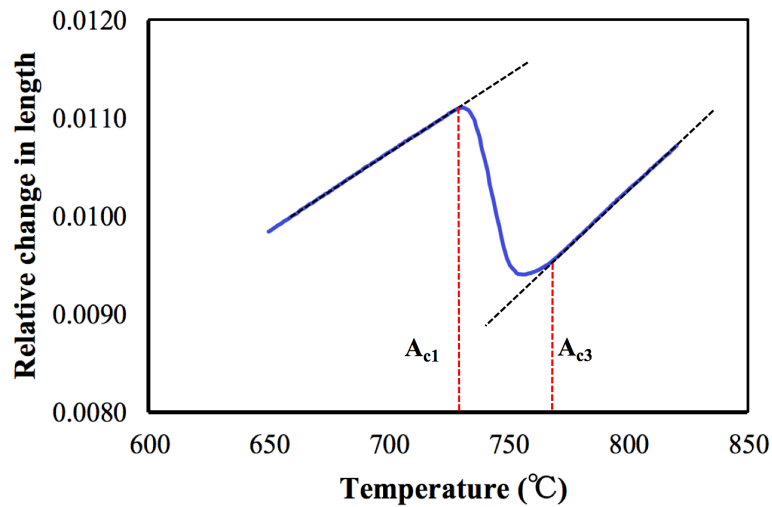


Figure 2.3: Determination of  $A_{c1}$  and  $A_{c3}$  temperatures using the linear extrapolation of FCC ( $A_{c3}$ ) and BCC lattice expansions ( $A_{c1}$ ).

Figure 2.2 and Figure 2.3 show the dilatometry curves obtained during cooling at 30 °C/s and heating at 5 °C/s respectively. Transformation temperatures such as martensite start temperature ( $M_S$ ), austenization start temperature ( $A_{c1}$ ) and austenization finish temperature ( $A_{c3}$ ) are determined from the dilatometry curves of the as quenched condition (Figure 2.2 and Figure 2.3) using the linear extrapolation of BCC and FCC expansions. The point at which the deviation from the linear extrapolation starts from the tangent is their respective transformation temperatures. The determined transformation temperatures  $M_S$ ,  $A_{c1}$  and  $A_{c3}$  are 245 °C  $\pm$ 5 °C, 735 °C  $\pm$ 5 °C and 774 °C  $\pm$ 5 °C respectively.

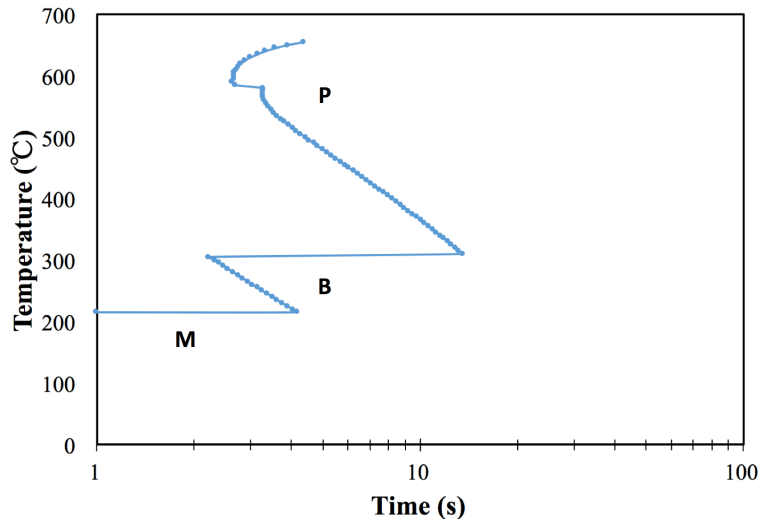


Figure 2.4: TTT diagram plotted for the current material. The diagram was plotted using the MUGC83 software from the University of Cambridge.

Figure 2.4 shows the TTT diagram for the current material calculated from the MUGC83 software from the University of Cambridge. Three regions have been marked in Figure 2.4 denoting three different phases (P- pearlite, B- bainite and M- martensite). The two horizontal lines in the figure denote the bainite start temperature ( $B_S \sim 300$  °C) and martensite start temperature ( $M_S \sim 220$  °C). The experimentally calculated value of  $M_S$  (245 °C) as shown in Figure 2.2 makes it clear that the accuracy of the software is poor.

### 2.3. Heat treatments

Heat treatments were done in dilatometry with cylindrical specimens of 3.5 mm diameter and 10 mm length which were machined from the hot rolled slab parallel to the rolling direction, comparable to the procedure in <sup>45</sup>.

There are eight different heat treatments designed for the current study, and they are presented in Figure 2.5. The heat treatment consists of two conditions above  $M_S$ , one condition exactly at  $M_S$  and five conditions below  $M_S$ . The idea behind this is to create conditions which does not have prior athermal martensite before the start of isothermal treatment (above  $M_S$ ) and conditions having different fractions of prior athermal martensite before the start of isothermal treatment (below  $M_S$ ) to study the effect of prior athermal martensite (PM) on the bainite formation kinetics. The nomenclature which will be used to represent the different isothermal treatments is Iso-xxx °C, where xxx represents the isothermal temperature.

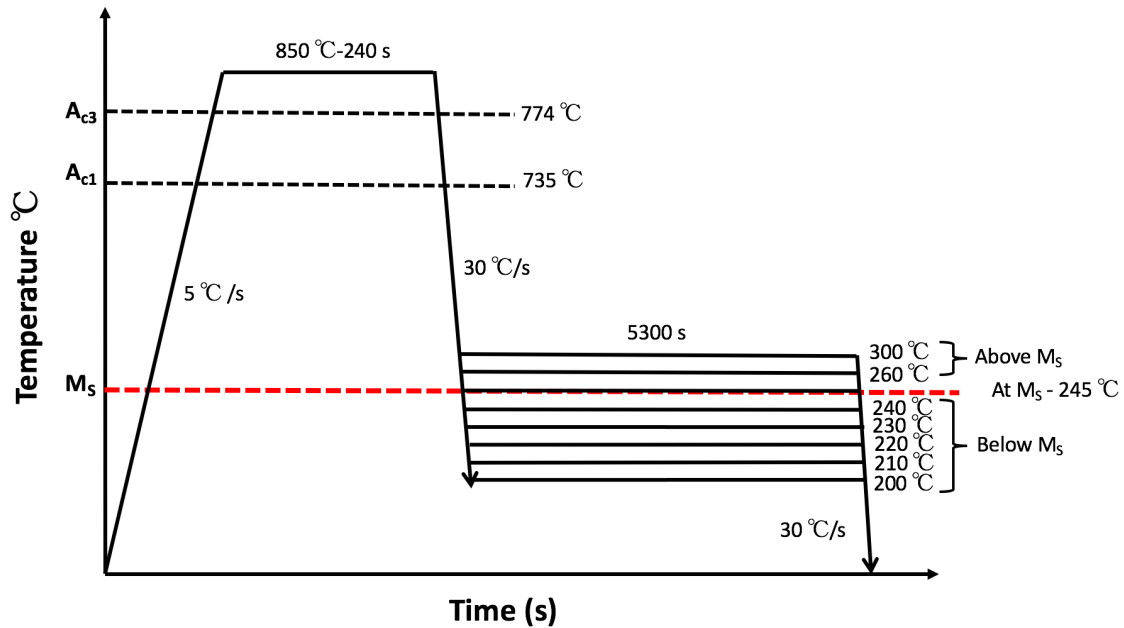


Figure 2.5: Schematic overview of the heat treatments used in the current study.

## 2.4. Dilatometry

### 2.4.1. Equipment

Dilatometry is one of the most powerful techniques for the research on solid-state phase transformations in steels since it allows the in-situ monitoring of the dimensional changes occurring in the sample which is closely related to the phase transformation and temperature during the application of thermal cycle<sup>46</sup>. The applicability of dilatometry is due to the change in specific volume (the ratio of volume to mass) of material during a phase transformation. When a steel undergoes a phase change, the lattice structure changes, e.g. from  $\alpha$  to  $\gamma$  while heated to the  $A_{c1}$  temperature. Due to the difference in the atomic volume between  $\alpha$  and  $\gamma$ , the phase transformation will be accompanied by the change in the specific volume, and this will be reflected as a sudden change in the length of the steel, as illustrated in Figure 2.3. When the steel is heated up, it expands linearly until it reaches  $A_{c1}$ , where the  $\alpha$  to  $\gamma$  transformation starts, a contraction is expected because of the smaller atomic volume of  $\gamma$ . When the temperature increases to  $A_{c3}$ , the steel is fully austenized and a further increase in temperature results in the linear expansion of the steel. The transformation temperatures can be identified by a sudden change in the length of the dilatometry curve.

A schematic representation of a push rod dilatometer is shown in Figure 2.6. The sample is clamped between two quartz push rods, and a Linear Variable Differential Transformer (LVDT) is used to record length changes in the sample and the push rods. A high-frequency induction coil is used to heat the sample and using small holes in the induction coil a cooling gas is supplied to cool the sample evenly. A thermocouple is used to record the temperature changes and to control the temperature of the sample.

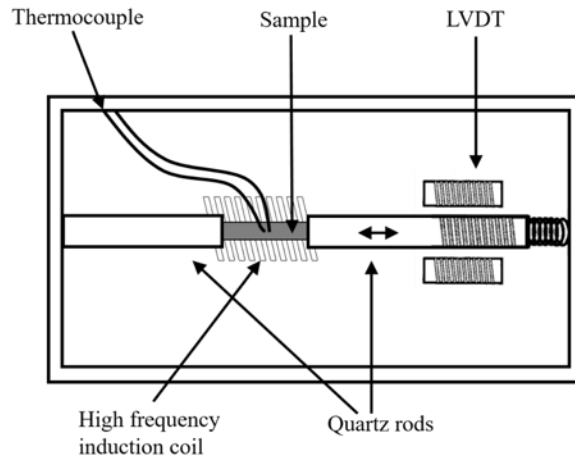


Figure 2.6: Schematic representation of the dilatometer configuration: Adapted from <sup>47</sup>.

The dilatometer used in the current study is Bahr 805 DIL A/D which has a length resolution of 50 nm. Heating rates of up to 100 Ks<sup>-1</sup> and cooling speeds of 100 Ks<sup>-1</sup> can be achieved. Solid cylindrical samples with a length of 10 mm and a diameter of 3.5 mm are used, with a type S thermocouple spot-welded on the surface. Vacuum on the order of 10<sup>-4</sup> mbar is applied during the heating and isothermal segments of the heat treatments. Helium has been used as the cooling gas. The initial length ( $L_0$ ) and the diameter ( $D_0$ ) of the sample are measured using a Mitutoyo digital calliper, model 500-181U, with a readout error of  $\pm 0.02$  mm.

As mentioned earlier, phase transformations are accompanied by a change in volume, but a dilatometer can only measure length change. The essential assumptions which relate volume change and the length change and allow for the study of phase transformations with a dilatometer are that the material behaves isotropically and that  $|\Delta V/V| \ll 1$ . These assumptions give rise to the relationship between length change and volume change as provided by:

$$\frac{3\Delta l}{l} \cong \frac{\Delta V}{V} \quad [1]$$

where,  $\Delta l/l$  is the length change of the specimen and  $\Delta V/V$  is the volume change of the specimen.

#### 2.4.2. Thermal expansion

In order to study the phase transformations in a dilatometer, the thermal expansion behaviour of the material needs to be determined. This can be extracted by the extrapolation of linear expansion behaviour of BCC and FCC lattices.

The linear lattice expansion derived from the model proposed by van Bohemen <sup>48</sup> can be used to obtain the thermal expansion of BCC and FCC lattices. Equations 2 and 3 gives the linear lattice expansion of austenite and ferrite respectively. The linear expansion coefficients have also been taken from the literature <sup>48</sup>. In the current study, linear expansion of FCC is obtained from the experimental curve of the as quenched condition (see Figure 2.2) but the

linear expansion of BCC has been extracted from van Bohemen<sup>48</sup> since the experimental curve of the as quenched condition is not complete in terms of BCC transformation (Figure 2.2). The calculated linear expansion of austenite (FCC) and ferrite (BCC) are plotted in Figure 2.7.

The linear lattice expansion of austenite (FCC) can be described as:

$$\frac{\Delta L^{\gamma}}{L_0^{\gamma}} = B_{\gamma}(T - \theta_D^{\gamma}) \quad [2]$$

where,  $\frac{\Delta L^{\gamma}}{L_0^{\gamma}}$  is the relative length change of an austenite lattice,  $B_{\gamma}$  is the thermal expansion coefficient of austenite,  $T$  the temperature and  $\theta_D^{\gamma}$  the Debye temperature\* of austenite.

The linear lattice expansion of ferrite (BCC) can be described as:

$$\frac{\Delta L^{\alpha}}{L_0^{\alpha}} = \frac{L_0^{\alpha} - L_0^{\gamma}}{L_0^{\gamma}} + B_{\alpha}(T - \theta_D^{\alpha}) \quad [3]$$

where,  $\frac{\Delta L^{\alpha}}{L_0^{\alpha}}$  is the relative length change of a ferrite lattice,  $B_{\alpha}$  is the thermal expansion coefficient of ferrite,  $\frac{L_0^{\alpha} - L_0^{\gamma}}{L_0^{\gamma}}$  is the relative change in length between the BCC and FCC lattices at 0 K,  $T$  the temperature and  $\theta_D^{\alpha}$  the Debye temperature of ferrite.

The thermal expansion behaviour of martensite does not differ significantly from ferrite<sup>49</sup>, so the thermal expansion of ferrite has been assumed for martensite here. The values are taken as  $B_{\gamma} = 24.8 \cdot 10^{-6} \text{ K}^{-1}$  and  $\theta_D^{\gamma} = 280 \text{ K}$ ,  $B_{\alpha} = 18.3 \cdot 10^{-6} \text{ K}^{-1}$ ,  $\theta_D^{\alpha} = 320 \text{ K}$  and  $\frac{L_0^{\alpha} - L_0^{\gamma}}{L_0^{\gamma}} = 103.9 \cdot 10^{-4}$ , all as described in<sup>48</sup>.

## 2.4.3. Quantification of phase fractions

### 2.4.3.1. Lever rule

Lever rule can be used to determine the phase fraction from the dilatometry data. The process is demonstrated as follows with the use of Figure 2.7.

---

\* The temperature of a crystal's highest mode of vibration is called as the Debye temperature.

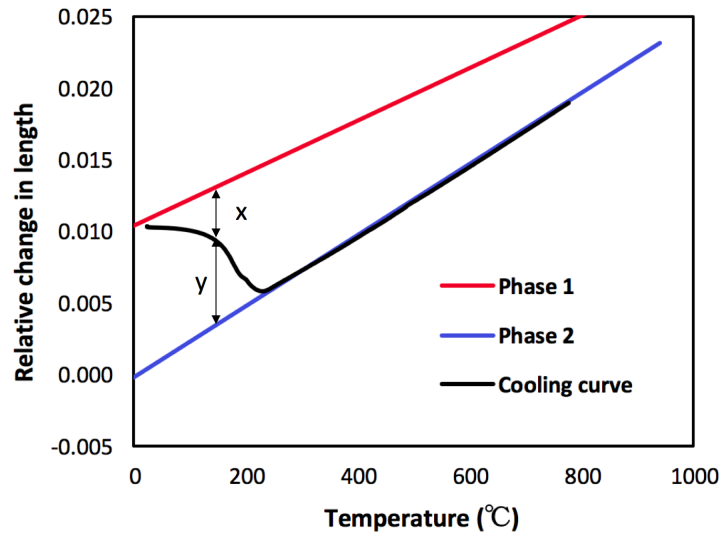


Figure 2.7: Lever rule to find out the phase fraction from the dilatometry data.

Let phase 1 be BCC and phase 2 be FCC in Figure 2.7. The fraction of phase 1 (ferrite) at temperature  $T$  is then  $\frac{y}{x+y}$ , while the fraction of phase 2 (austenite) at temperature  $T$  is  $\frac{x}{x+y}$ . The lever rule could also be applied during isothermal transformations.

#### 1.1.1.1. Koistinen- Marburger equation

The Koistinen-Marburger model (Equation 4) describes well the martensitic transformation below  $M_S$  temperature<sup>50</sup> and it has been used to fit the experimental martensitic transformation curve obtained from the as quenched condition (Figure 2.2). It is an exponential law where the  $f_m$  depends on two fitting parameters:  $\alpha_m$  and  $T_{km}$ . The fitting parameters are compositional dependent according to van Bohemen et al.<sup>51</sup>.

$$f_m = 1 - \exp[-\alpha_m(T_{km} - T)] \quad [4]$$

where,  $\alpha_m$  is the rate parameter and  $T_{km}$  is the theoretical martensite start temperature.  $T_{km}$  is generally lower than the experimental  $M_S$ .

#### 2.4.4. ‘Zero’ point for Bainite transformation

The analysis of experimental kinetic curves of the isothermal formation of bainite requires a “zero” (start) time and the change in length to be established. There are two different conditions for the zero point for treatments performed above  $M_S$  and below  $M_S$  as shown in Figure 2.8 (a) and Figure 2.8 (b) respectively.

The start (zero point) of the isothermal expansion for the isothermal treatments above  $M_S$  is considered to be the point at which the minimum change in length becomes positive (Figure 2.8(a)). For conditions below  $M_S$ , the start of the isothermal transformation corresponds to the point at which the temperature reaches a minimum value during the cooling when the athermal martensite stops forming making the dilatation after that to be considered as the



dilatation due to the formation of bainite (Figure 2.8(b)). These two zero points for above  $M_S$  and below  $M_S$  are denoted in Figure 2.8(a) and (b) with a red marker. It has to be noted that the zero point will vary per treatment. The scatter in the plots have been removed for plotting the kinetic curves applying the cubic spline interpolation to the measured dilatometry length data in order to obtain a value for a fixed incremental time interval. It was followed by the smoothening of the curves using the moving average method.

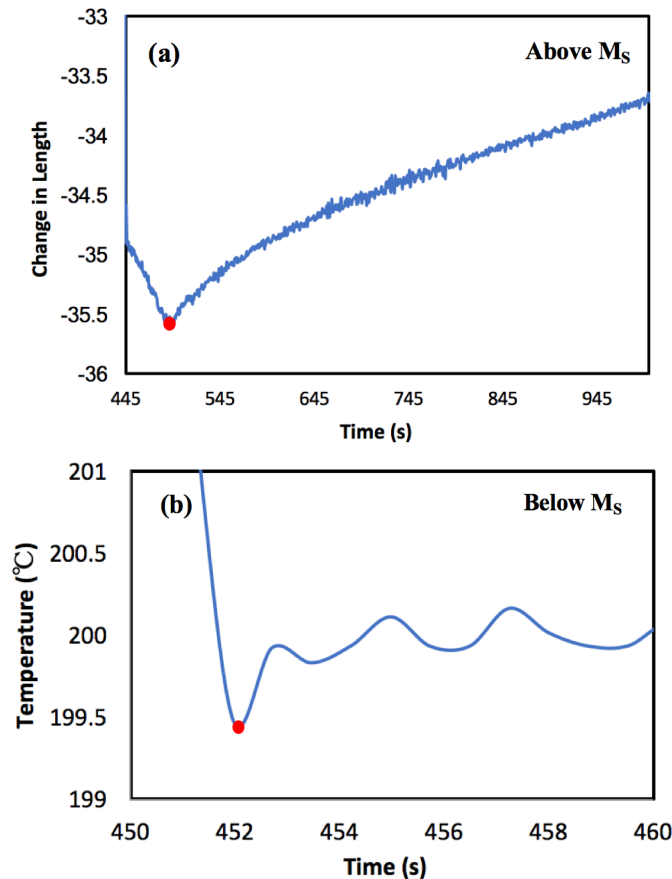


Figure 2.8: The zero point for the start of the bainite transformation for above  $M_S$  and below  $M_S$  isothermal conditions are marked in the graphs with a red point on the plot. The plot on the top is for above  $M_S$  and the plot below is for below  $M_S$  conditions.

## 2.5. Metallographic preparation

Once the heat treatments were done in the dilatometer, the samples were cut in the middle as shown in Figure 2.9 for further studies by X-ray diffraction, optical microscopy, scanning electron microscopy and hardness measurement. One-half of the sample has been used for the X-ray diffraction and hardness measurements, and the other half of the sample has been utilised for the optical microscopy and scanning electron microscopy. For all the purposes, only the inside surface (i.e. the cut surface at the centre of the full sample) has been used after proper polishing of the surface.

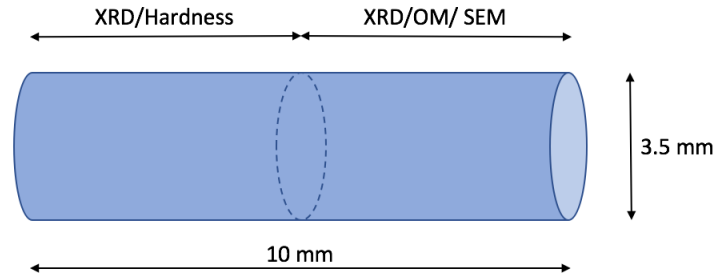


Figure 2.9: Schematic of the usage of the sample for various characterization and their cutting scheme.

Table 2.2: Overview of the sample preparation with regards to the polishing of the sample.

Grinding material	Polishing quality ( $\mu\text{m}$ )	Time (min)
SiC – P180	75	1
SiC – P320	46	1
SiC – P800	21.8	1.5
SiC – P1200	15.2	1.5
SiC – P2000	10	1.5
Diamond suspension ( $3\mu$ )	3	5
Diamond suspension ( $1\mu$ )	1	4

Table 2.2 shows the complete overview of the sample polishing process with the polishing step, polishing quality and the time consumed at each stage. The arrow in the table indicates the start and end of the whole process.

## 2.6. X-ray Diffraction (XRD)

X-ray diffraction is a technique to investigate the fine structure of the matter<sup>52</sup>. This technique can be used to determine crystal structures, the volume fractions of different phases, chemical analysis and stress measurement.

Planes of atoms within a material will diffract beams of X-rays at specific angles, and these diffracted beams are commonly used to characterize various material properties. There are two features associated with the diffracted beams that are used: the angle between the incident and diffracted beams ( $2\theta$ ) and the intensity of the diffracted beam ( $I$ ) as shown in Figure 2.10.

Bragg’s law relates the angle ( $\theta$ ), the wavelength of the beam ( $\lambda$ ) and the spacing between the planes of atoms in the material ( $d$ ):

$$n\lambda = 2d \cdot \sin\theta \quad [5]$$

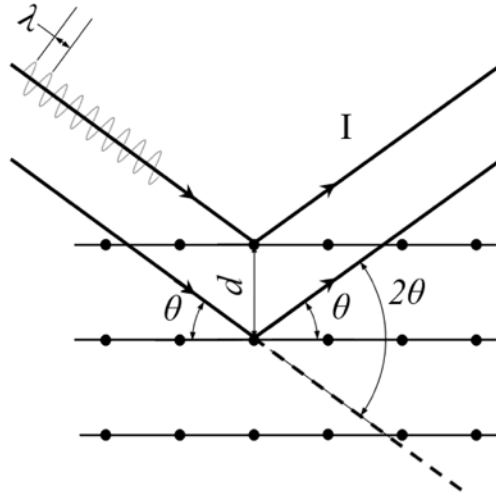


Figure 2.10: Schematic representation of Bragg diffraction of crystallographic planes<sup>52</sup>.

In the current study, the X-ray diffraction measurements have been carried out at room temperature on a Bruker D8-Advanced diffractometer equipped with a Vantec Position Sensitive Detector (PSD). CoK $\alpha$  radiation has been used, and  $2\theta$  scans have been performed with a step time of 0.6 seconds and a step size of  $0.025^\circ$ .  $2\theta$  values range from  $40^\circ$  to  $130^\circ$ , containing four ferrite and four austenite peaks.

The EVA software suite (DIFFRAC<sup>plus</sup> Evaluation Package, version 2.2) has been used to analyse the diffraction peaks. The volume fraction of retained austenite is determined from the integrated intensities of austenite and ferrite peaks using the method described in<sup>53</sup> with:

$$f_{\gamma R} = \frac{\frac{1}{n_\gamma} \sum_1^{n_\gamma} \left( \frac{I_\gamma^{hkl}}{R_\gamma^{hkl}} \right)}{\frac{1}{n_\alpha} \sum_1^{n_\alpha} \left( \frac{I_\alpha^{hkl}}{R_\alpha^{hkl}} \right) + \frac{1}{n_\gamma} \sum_1^{n_\gamma} \left( \frac{I_\gamma^{hkl}}{R_\gamma^{hkl}} \right)} \quad [6]$$

where,  $I_\gamma^{hkl}$  and  $I_\alpha^{hkl}$  are the integrated intensities of austenite and ferrite peaks respectively;  $n_\gamma$  and  $n_\alpha$  are the numbers of  $\{hkl\}$  lines for which the integrated intensities have been measured;  $R_\gamma^{hkl}$  and  $R_\alpha^{hkl}$  are the theoretical intensities<sup>53</sup> as presented in Table 2.3.

Table 2.3: Theoretical line intensities (R values) for the ferrite and austenite phases for Co radiation ( $\lambda=1.79021\text{\AA}$ ).

$\{hkl\}_{\text{phase}}$	$\{110\}_\alpha$	$\{200\}_\alpha$	$\{211\}_\alpha$	$\{220\}_\alpha$	$\{111\}_\gamma$	$\{200\}_\gamma$	$\{220\}_\gamma$	$\{311\}_\gamma$
<b>R</b>	109.9	14.5	30.9	14.4	85.2	37.0	20.4	30.1

There are two different errors from the XRD measurements. The statistical error represents the error due to the scatter in the XRD spectrum, and the  $I/R$  error is based on the relative peak intensities between all the four peaks of austenite and ferrite. These two errors must be added together for the representation of error since they are from two different sources.



Figure 2.11: Schematic of the mounting of the sample on the Si wafer {510} for XRD measurement.

The surface preparation for XRD is the same as mentioned in Table 2.2. The polished sample was mounted over the Si{510} wafer as shown in Figure 2.11 such that the top of the cylinders is aligned with the goniometer axis. The inside surface (i.e. the cut surface at the centre of the sample) was polished and used for all the characterization purposes as mentioned already. Both the surfaces of two halves are used for the measurement to obtain a larger number of counts.

## 2.7. Optical Microscopy

The same procedure for the sample polishing was used as mentioned earlier in Table 2.2. The samples were first mounted into a conductive thermosetting resin (Polyfast) and then was followed by the grinding and polishing process. The samples were later etched with 2% Nital solution for 8 seconds. The mounting along with the sample is shown in Figure 2.12.



Figure 2.12: Sample mounted with conduction polyfast resin and polished.

The device used for optical microscopy is Olympus BX60M with the magnifications of 10x, 50x and 100x. The larger microstructural features can be identified using the optical microscopy. In this study, it has been used to characterize the microstructural banding structure due to the inhomogeneous distribution of Mn. This will be dealt in detail in the results section.

## 2.8. Scanning Electron Microscopy (SEM) and Energy Dispersive X-ray Spectroscopy (EDS)

The sample preparation used for the optical microscopy was carried to the SEM characterization. The SEM was performed using the JEOL JSM-6500F series field emission gun SEM, using the secondary electron imaging detector. The accelerating voltage was 15 kV and the nominal working distance was 10 mm. The SEM images revealed the fine microstructures of bainite, austenite, martensite and carbides which will later be shown in the results section.

The banding effect due to the presence of Mn has been studied using the EDS analysis. EDS is an analytic technique used for the elemental analysis or chemical characterization of the material<sup>54</sup>.

## 2.9. Micro-hardness Vickers measurements

Micro-hardness Vickers tests were done on heat-treated samples as a measurement of their strength. The micro hardness measurements for the current research were done in the samples which were polished until 1  $\mu\text{m}$  but not etched. The measurements were done in Struers Durascan machine with a diamond indenter. The diamond indenter makes an indent from which the diagonal distance ( $d$ ) can be calculated and used in the Equation 7 to find the Vickers hardness along with the value of force applied on the sample. An example of indentation is shown in Figure 2.13 along with the lines to measure the dimensions of the indent. The load used in this study for all the samples is 0.5 Kg.

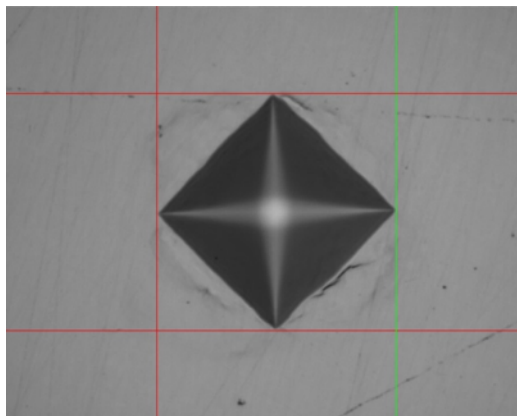


Figure 2.13: Picture of the indent made by the diamond indenter on the sample and the lines representing the measure of the size of the indent.

Several measurements (~5) per sample were carried out and the results are expressed as mean values and standard deviation.

$$HV = \frac{F}{A} \quad [7]$$

where,

$$A \approx \frac{d^2}{1.8544} \quad [8]$$

where,  $F$  is the force applied and  $d$  is the distance between the opposite edges of the indent.

# 3. Results and Discussion

## 3.1. Overview

This chapter will present the results and their respective discussion from dilatometry, XRD, optical microscopy, scanning electron microscopy, EDS and micro-hardness Vickers measurements. The effect of the PM on the bainite transformation kinetics based on the nucleation rates will also be discussed in detail. At the end of the section, the comparison of the effect of PM on bainite transformation kinetics with varying carbon content will be presented.

## 3.2. Dilatation Analysis of Phases

### 3.2.1. Characterization of Martensitic Transformation

Figure 3.1 shows the evolution of volume fraction of martensite as a function of temperature for the as quenched condition cooled at 30 °C/s (see Figure 2.2). The experimental curve has been fitted with the K-M model (as shown in Section 1.1.1.1). The found fitting parameters are  $T_{km} = 214$  °C and  $\alpha_m = 0.0132$  K<sup>-1</sup>. The difference between the experimental curve and fitting curve has been found to be around 10%. As described by van Bohemen<sup>51</sup>, the discrepancy between the experimental  $M_S$  and  $T_{km}$  can be explained by an initial gradual transformation during the start of the martensite transformation, which is not incorporated by the exponential KM model. Typically, the  $T_{km}$  is 5-20 °C lower than the  $M_S$ <sup>51</sup>.

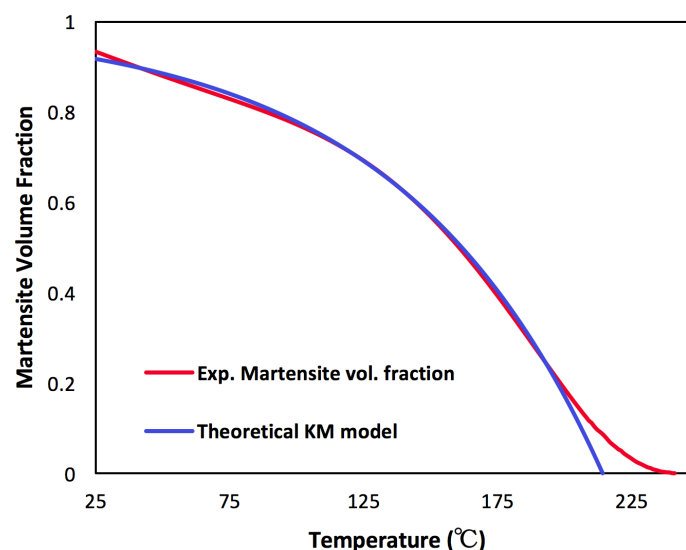


Figure 3.1: Evolution of volume fraction of martensite as a function of temperature for experimental quench condition and theoretical Koistinen- Marburger equation fitted for the experimental data.

### 3.2.2. Identification of Phases from the Dilatation Data

As seen in Figure 2.5, there are conditions above and below  $M_S$ , which means that the phases formed will be slightly different in both conditions. In order to figure out the various phases formed at different stages of the heat treatment, the dilatation data from dilatometry can be used. The relative change in length as a function of temperature for conditions above and below  $M_S$  has been represented in Figure 3.2 and Figure 3.3 respectively. For the better representation of the phases formed at different stages, one condition each from the above and below  $M_S$  conditions have been selected and represented in Figure 3.2 and Figure 3.3.

In the case of isothermal treatments above  $M_S$  (Figure 3.2), a positive dilatation is observed at the start of the isothermal treatment, and it represents the formation of bainitic ferrite (BF). Then at the end of isothermal treatment, the positive dilatation stops and the dilatation starts to become negative when the final cooling begins. At some point during the final cooling, the fresh martensite (FM) starts forming from the untransformed austenite (unstabilized austenite) which gives a change in slope (as pointed by the deviation of the dashed line). From the dilatation data, it is clear that the phases formed in the conditions above  $M_S$  are bainitic ferrite (BF) and fresh martensite (FM). It has to be noted that the austenite which is sufficiently stabilised will be retained at the end of the final cooling.

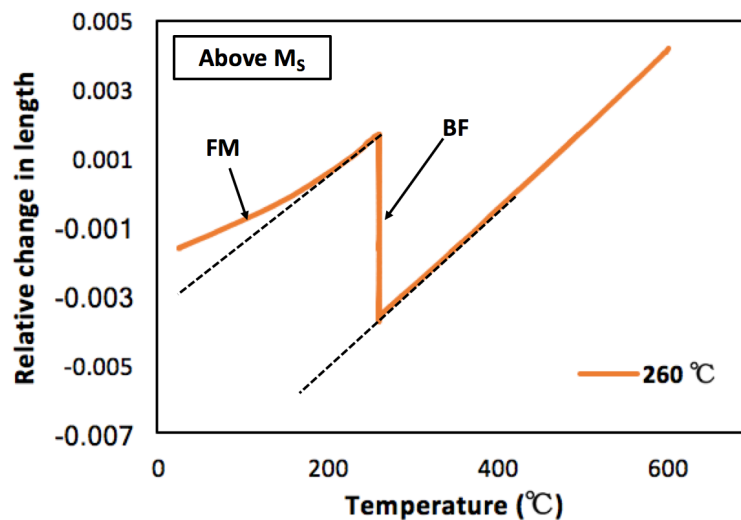


Figure 3.2: Phase identification from the dilatation data of isothermal treatment at 260°C (above  $M_S$ ) from dilatometry. BF- Bainitic Ferrite & FM- Fresh Martensite.

In the case of isothermal treatments below  $M_S$  (Figure 3.3), a small positive deviation from the linear contraction is observed before the start of the isothermal treatment. This positive dilatation represents the formation of prior athermal martensite (PM) since the isothermal treatment is below  $M_S$ . The formation of PM is observed to be ceased when the isothermal temperature is reached. The formation of the BF and FM is observed after the formation of PM. The change in slope (FM) and dilatation (BF and PM) with the formation of all three phases are observed to be positive because of the transformation from FCC to BCC or BCT.



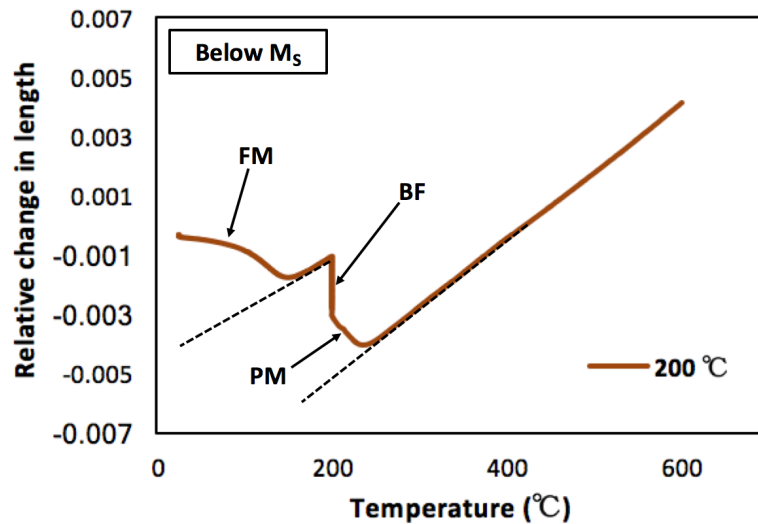


Figure 3.3: Phase identification from the dilatation data of isothermal treatment at 200 °C (below  $M_S$ ) from dilatometry. PM- Prior athermal Martensite, BF- Bainitic Ferrite & FM- Fresh Martensite.

Figure 3.4 and Figure 3.5 show the relative change in length as a function of temperature for all conditions above and below  $M_S$  temperature respectively. The curves have been plotted along with the as-quenched dilatation curve for comparison. It can be seen that the dilatation due to the formation of BF corresponds well with the isothermal temperatures. In Figure 3.4, the change in slope due to the formation of FM is observed to be small during the final cooling for all three conditions which mean that the isothermal transformation is almost complete in these conditions. From Figure 3.5, it can be observed that the dilatation due to the formation of PM increases with the decrease in isothermal temperature below  $M_S$  and it corresponds well with the martensite transformation curve in the as-quenched condition (see Figure 2.2). The dilatation during the final cooling is observed to be increasing for the conditions Iso-210 °C and Iso-200 °C (Figure 3.5) which mean that a higher volume fraction of FM is formed when compared to the other conditions. This denotes that the isothermal transformation is an incomplete stage in these two cases.

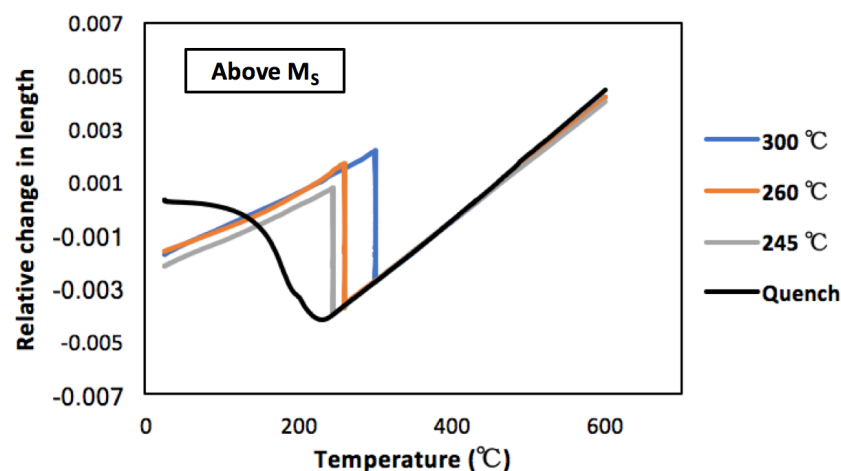


Figure 3.4: Relative change in length as a function of temperature for isothermal treatments above and just at  $M_S$  (300 °C, 260 °C & 245 °C).

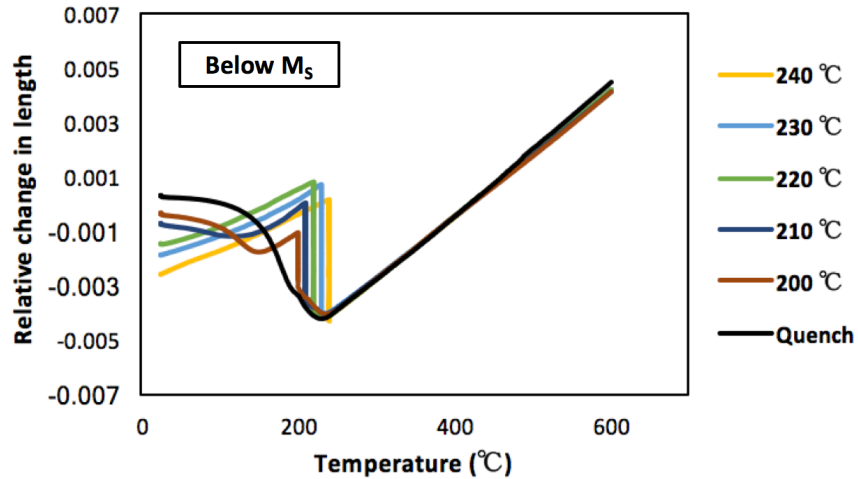


Figure 3.5: Relative change in length as a function of temperature for isothermal treatments below  $M_S$  (240 °C, 230 °C, 220 °C, 210 °C & 200 °C).

### 3.3. Quantification of Phases

It is quite clear from the previous section that the phases which are expected from the heat treatments (Figure 2.5) are prior athermal martensite (PM) (only in below  $M_S$  conditions), bainitic ferrite (BF), retained austenite (RA), fresh martensite (FM), and carbides (presence of carbides will be discussed in Section 3.4). The quantification of all these phases is essential to understand the microstructural evolution. Here, the volume fraction of FM and PM (from the as-quenched data, see Figure 2.2) are found using the dilatation data and the volume fraction of RA is found using the X-ray diffraction. The fraction of BF is obtained by balancing the volume fractions of the other three phases as shown in Equation 9.

$$f^{BF} = 1 - f^{PM} - f^{FM} - f^{RA} \quad [9]$$

#### 3.3.1. Volume Fraction of Retained Austenite (RA) from XRD

Figure 3.6 shows the XRD spectrum for all the isothermal conditions along with the ferrite and austenite peak labels. The  $\{111\}$  austenite peak overlaps with the  $\{110\}$  ferrite peak for all the isothermal temperatures which makes it difficult to measure the area under the  $\{111\}$  austenite peak accurately. Therefore,  $\{111\}$  austenite peak has been omitted from the area calculations. For the same reason, the area of  $\{110\}$  ferrite peak has been slightly overestimated since it includes the area of  $\{111\}$  austenite peak too.

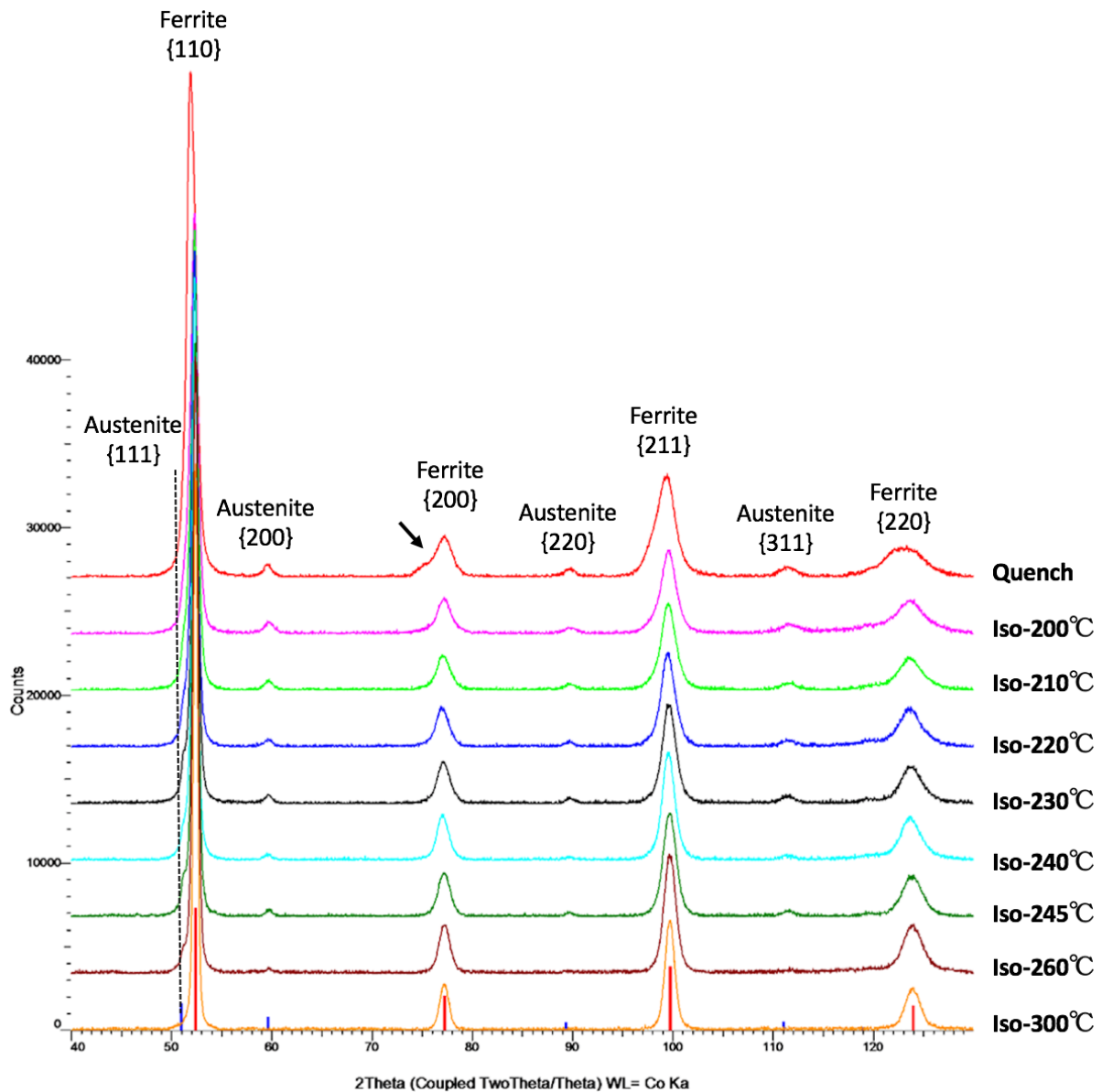


Figure 3.6: XRD spectrum for all the conditions. The blue indicators show the austenite peaks  $\{111\}$ ,  $\{200\}$ ,  $\{220\}$  &  $\{311\}$  respectively. The red indicators show the ferrite peaks for  $\{110\}$ ,  $\{200\}$ ,  $\{211\}$  and  $\{220\}$  respectively.

It can be observed from the Figure 3.6 that the  $\{200\}$  ferrite peak of the as-quenched sample has an apparent peak splitting (denoted by an arrow in the figure). This peak splitting can be related to the martensite in BCT structure rather than a BCC structure due to insufficient time for the carbon atoms to diffuse out. The two lattice parameters ( $a$  and  $c$ ) in the BCT structure creates the peak splitting in the case of the as-quenched sample. Peak splitting is not observed in the other conditions since the martensite which is formed during the initial cooling is tempered during the isothermal treatment leading to a structural change from BCT to BCC. Fresh martensite, which is formed in other conditions is very less in fraction when compared to the as-quenched sample. This makes the peak splitting relatively very difficult to observe in the other conditions.

Peak broadening can be seen for  $\{200\}$  ferrite peak in all conditions below  $M_S$ . This effect is shown in Figure 3.7, where the Iso-200°C (below  $M_S$ ) and Iso-300°C (above  $M_S$ ) are compared. The peak broadening could be because of two potential reasons:

1. Fresh martensite (FM) will have a BCT structure with two lattice parameters ( $a$  and  $c$ ) giving rise to peak splitting which would eventually lead to an asymmetric peak broadening. The volume fraction of FM formed in Iso-200°C is higher when compared to that of the condition Iso-300°C. This might reason because of which the peak broadening is predominant in the condition in Iso-200°C when compared to the condition Iso-300°C. (Note: a slight asymmetry is visible in Iso-200°C condition).
2. The second reason might be because of dislocation density in the martensite units where the  $d$ -spacing will be different at different positions of the sample which will result in the peak broadening. It is well known that the presence of higher amount of fresh martensite will increase the dislocation density<sup>12</sup>. Hence, the condition Iso-200°C must have higher dislocation density than that of the Iso-300°C. This may have led to the symmetrical peak broadening in the case of Iso-200°C.

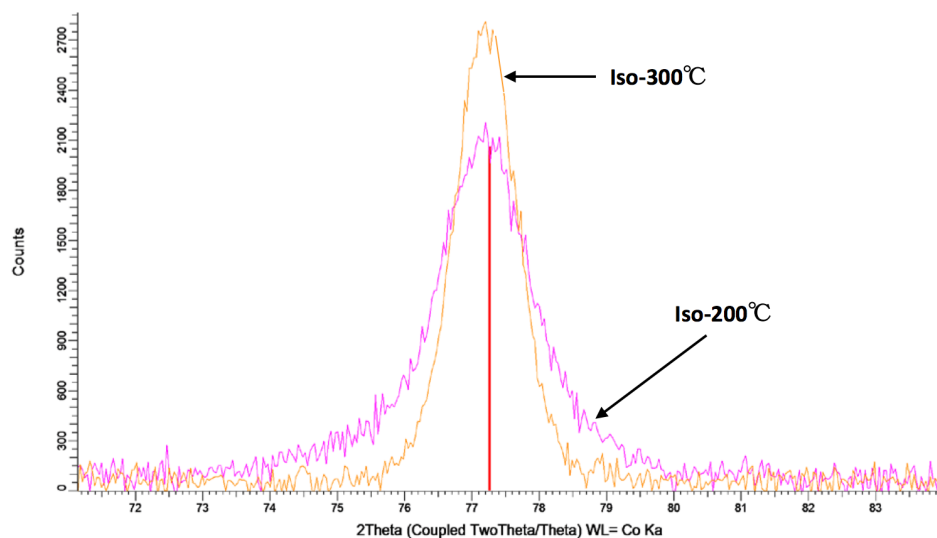


Figure 3.7: Comparison of  $\{200\}$  ferrite peak reflection for the conditions Iso-300 °C and Iso-200 °C.

The determined volume fraction of retained austenite (RA) for all the conditions is shown in Section 3.3.3. More details on XRD calculation can be found in Appendix 7.1.

### 3.3.2. Volume fraction of Fresh Martensite (FM) and Prior Athermal Martensite (PM) from Dilatometry

Figure 3.8 shows the dilatometry curve (relative change in length as a function of temperature) corresponding to the Iso-200 °C condition and the procedure to determine the

volume fraction of FM. The volume fraction of fresh martensite (FM) can be determined by comparing the red double arrow and the black double arrow shown in Figure 3.8. The red double arrow denotes the maximum net dilatation with respect to the austenite phase obtained at the room temperature in the as-quenched treatment. The black double arrow indicates the net dilatation for the isothermal treated condition. The net dilatation (black double arrow) is obtained by estimating the difference of change in length between the experimental curve and the extrapolated line (dashed line). This dashed line is the representation of the linear change in length if there is no martensitic transformation while cooling to RT. The volume fraction of PM is determined from the experimental curve of the as-quenched specimen (Figure 2.2) using the lever rule.

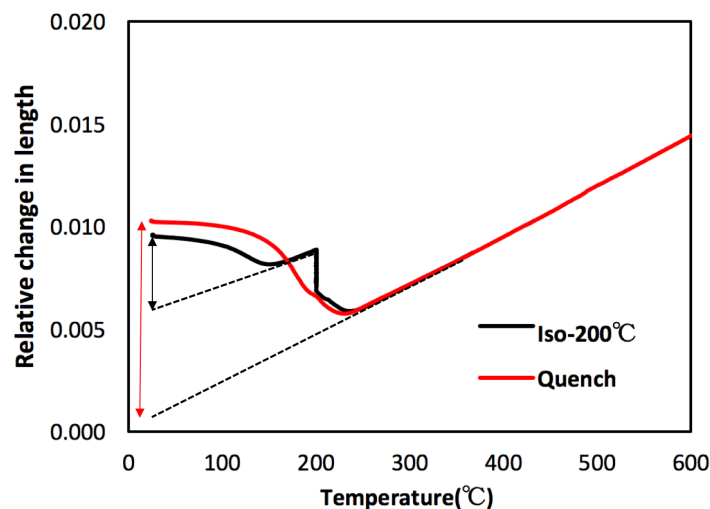


Figure 3.8: Method to determine the fraction of fresh martensite from the dilatation data of dilatometry. The black double arrow represents net dilatation at RT, and the red double arrow shows the maximum net dilatation at RT.

### 3.3.3. Summary of the Phase Fractions

Figure 3.9 shows the summary of the phase fractions obtained from the dilatometry (PM and FM) and XRD (RA) for all the conditions (error for the fractions are given in Appendix 7.2). The main observations from Figure 3.9 are as follows:

- **Bainitic ferrite (BF):** For the conditions above  $M_S$ , the volume fraction of bainitic ferrite increases with decreasing isothermal temperature reaching its maximum around  $M_S$  temperature. For the conditions below  $M_S$ , the volume fraction of bainitic ferrite decreases with decreasing isothermal temperature (except the condition Iso-220°C) reaching a minimum fraction of 0.31 for the Iso-200°C condition. These volume fractions of bainite are later used in Section 3.6 to represent the evolution of volume fraction of bainite as a function of time.
- **Retained austenite (RA):** The slight variation in the volume fraction of retained austenite could be related to the volume fraction of bainitic ferrite. This is because,

bainitic ferrite and prior athermal martensite contain carbides (see Section 3.4) which act as the reservoir for the carbon and stops the partitioning of carbon to the austenite, leaving out the austenite without sufficient stabilisation. Thus, the increase in the volume fraction of BF and PM reduces the volume fraction of retained austenite in the material. Since the volume fraction of BF is relatively higher than the PM, the effect due to the volume fraction of BF will be more significant here.

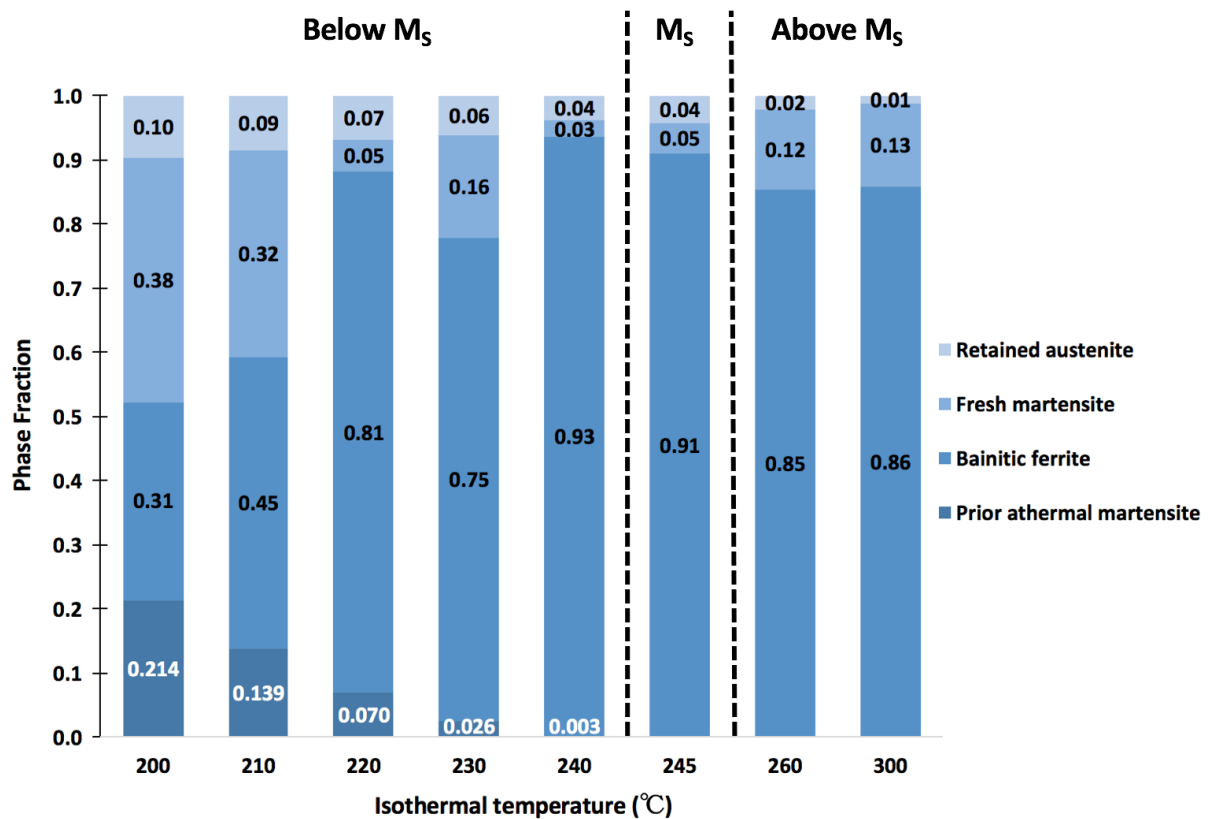


Figure 3.9: Summary of the phase fractions for all the conditions.

- Prior athermal martensite (PM):** As mentioned earlier, the volume fraction of PM increases with the decrease in the isothermal temperature below  $M_S$ , which is consistent with the experimental martensitic transformation curve (Figure 3.1). The maximum volume fraction of PM reached is 0.21 for the condition Iso-200 °C which is 45 °C less than the  $M_S$  temperature.
- Fresh martensite (FM):** There seems to be a trend with the volume fraction of FM (except for the condition Iso-220°C) since it increases with the decrease in temperature below  $M_S$ . This is because the volume fraction of bainite formed during the isothermal treatment in conditions like Iso-210°C and Iso-200°C is relatively smaller which leaves out a significant fraction of untransformed austenite before the final cooling. Thus only the stabilised austenite is retained (which is around 0.10 in volume fraction) and the rest of the untransformed austenite, which is not sufficiently stabilised, transforms into FM during the final cooling to RT.



### 3.4. Microstructural Characterization

Figure 3.10 shows the optical micrograph of some of the conditions above  $M_S$  (Iso-260°C), exactly at  $M_S$  (Iso-245°C) and below  $M_S$  (Iso-230°C, Iso-210°C and Iso-200°C).

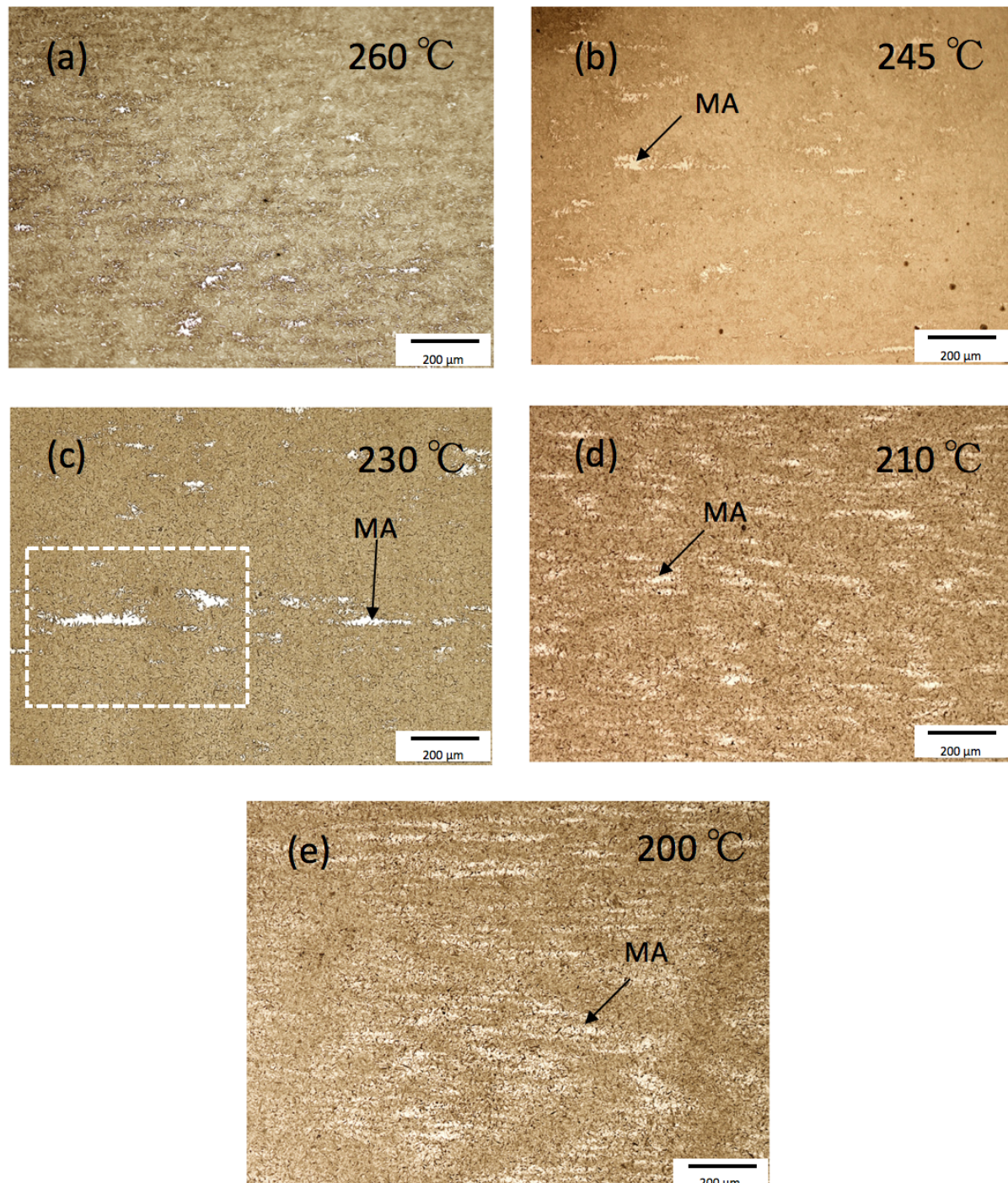


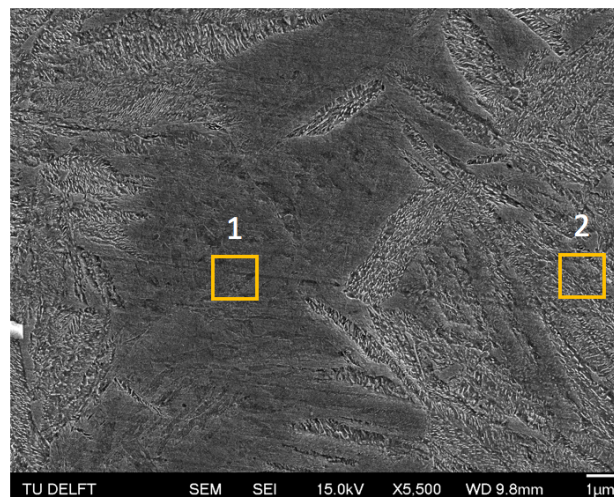
Figure 3.10: Optical micrographs of Above  $M_S$ : (a) 260 °C, At  $M_S$ : (b) 245 °C, Below  $M_S$ : (c) 230 °C (d) 210 °C (e) 200 °C. Apparently, banding of Mn is seen in all the conditions (Arrows denote the MA islands). The Isothermal temperature is labelled at the top right of the micrographs.

The dark etched regions represent the bainitic ferrite and the lighter areas (pointed by arrow) represent RA/FM which are commonly called as MA island<sup>55</sup>. These microstructural

islands are seen in the Figure 3.10 (a), (b) and (c) due to chemical banding in the material. Chemical banding is common in hot rolled and cold rolled steels with high alloy content<sup>56</sup>. It is related to the dendritic solidification during which the segregation of the substitutional alloying elements happens. During the hot rolling, the formation of chemical banding will be seen in the regions with different segregation levels, and the chemical bands will be aligned parallel to the rolling direction.

In the current case, the Mn content and segregation of Mn are responsible for the chemical heterogeneity in the material. As explained by C. Goulas et al.<sup>55</sup>, manganese is a  $\gamma$  stabiliser and reduces the  $A_{C3}$  temperature and local  $M_S$  temperature. Thus the PM will first form in the regions where the Mn content is lower. The formation of the bainitic ferrite will also start in the areas with lower Mn content. During the final cooling to the RT, the remaining untransformed austenite (areas with high Mn content) transforms into fresh martensite, and a small fraction of untransformed austenite which is sufficiently stabilised gets retained as RA. Thus the compositional variation is the key to the formation of MA islands in the microstructure. The evidence for this heterogeneous distribution of Mn and the formation of MA islands in the Mn rich region is given in the Figure 3.11.

Figure 3.11 shows the EDS measurement for the condition Iso-230°C. Two areas (area-1: inside the MA island and area-2: outside the MA island) were measured using EDS and the area inside the MA island is observed to have more Mn than that of the area outside the MA island, as shown in the table in Figure 3.11. Note that the region with a smooth surface after etching is the MA island.



Area	Fe (wt%)	Mn (wt%)
1 (Banding)	95.65	3.60
2	97.22	2.01

Figure 3.11: Mn segregation studied through EDS. The table on the bottom shows the Mn wt% for the two different areas selected (1-inside the MA island and 2-outside the MA island) in the image from SEM.



The microstructural banding and the MA islands are observed to have a larger area in the conditions Iso-210°C and Iso-200°C (see Figure 3.10 (d) and (e)) when compared to the other three conditions. This can be related to the higher volume fraction of fresh martensite (FM) in the conditions Iso-210°C and Iso-200°C (0.32 and 0.38 respectively) when compared to the other three conditions (see Figure 3.9). Figure 3.12 shows the magnified image of MA islands from condition Iso-230°C.

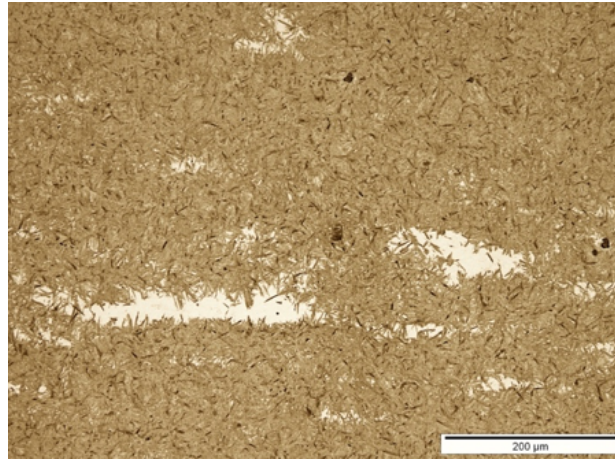


Figure 3.12: Magnified version of the white dotted box in the Figure 3.10 (c) showing the banding effect.

Figure 3.13, Figure 3.14 and Figure 3.15 show the SEM images for three isothermal conditions above, exactly at and below  $M_S$  respectively. The identified microstructural features are labelled with an arrow on the images.

For above  $M_S$  condition (Iso-260°C) (Figure 3.13), acicular units with carbides precipitated inside them are observed. The carbides are seen to be aligned parallel inside a single acicular unit which is a characteristic feature of lower bainite. Thus the BF formed here is the lower bainite and is expected to form at these isothermal temperatures for the composition of the material under study (see Figure 1.6). The interlath structure which is observed between the BF units can be identified as RA. These are mostly found in between two BF units since the carbon partitioned to the untransformed austenite during the formation of the lower bainite stabilises the untransformed austenite in between two BF units resulting in the retention of that region of the untransformed austenite. There are few large areas of smooth surface after etching in the microstructure which are identified as MA islands<sup>23</sup>.



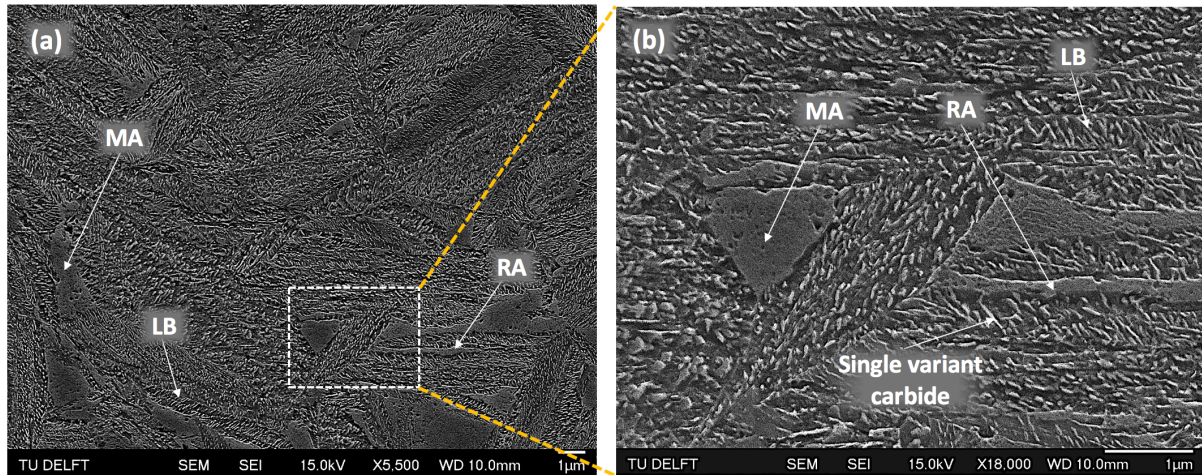


Figure 3.13: SEM micrographs of the microstructure obtained in a condition isothermally treated above  $M_S$  at  $260^\circ\text{C}$  for 5300s. Here, LB- lower bainite, MA- martensite austenite islands and RA- retained austenite. The figure on the right is the magnified version of the white box shown in the left figure.

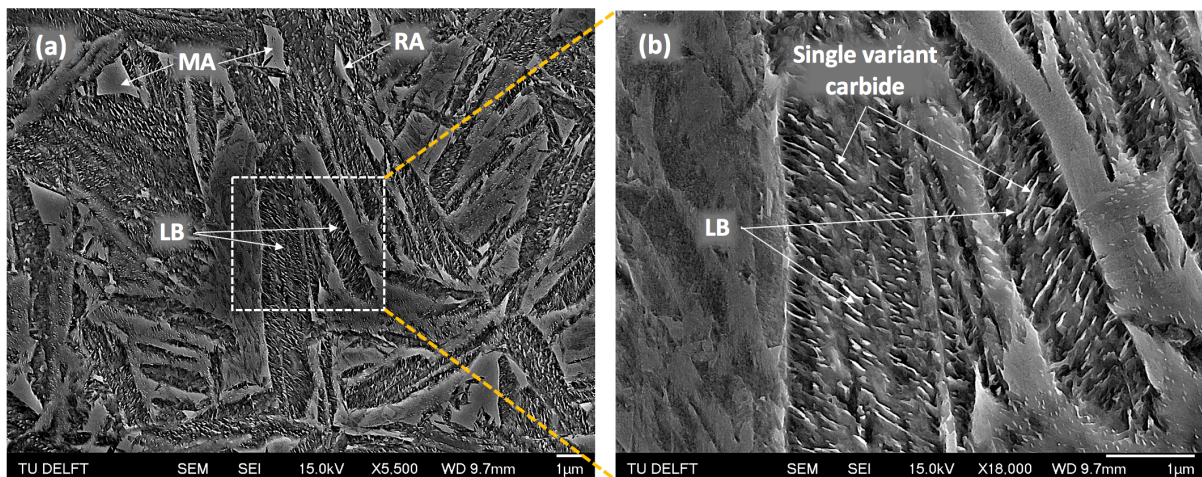


Figure 3.14: SEM micrographs of the different microstructures obtained in a condition isothermally treated exactly at  $M_S$  at  $245^\circ\text{C}$  for 5300s. Here, LB- lower bainite, RA- retained austenite and MA- martensite austenite islands. The figure on the right is the magnified version of the white box shown in the left figure.

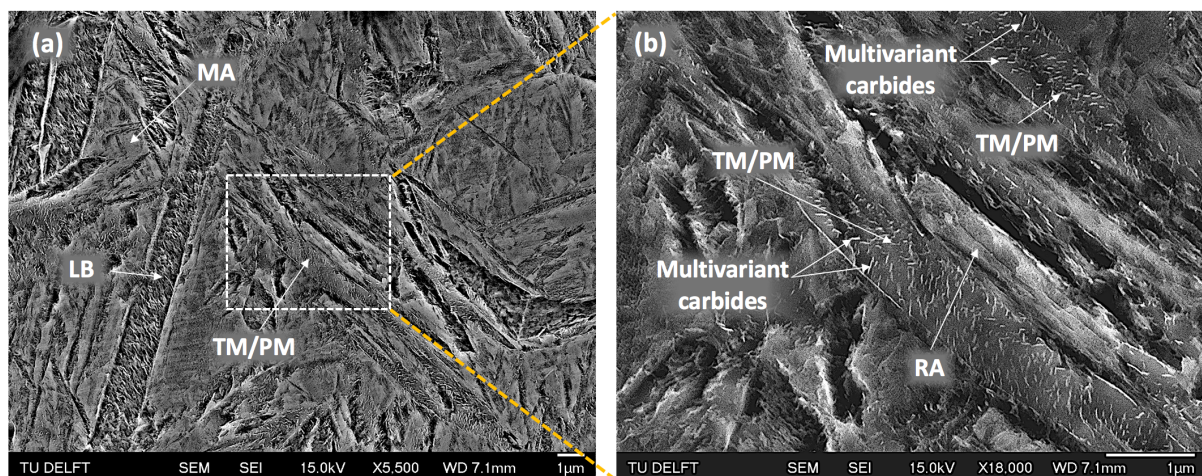


Figure 3.15: SEM micrographs of the microstructures obtained in a condition isothermally treated below  $M_S$  at  $200^\circ\text{C}$  for 5300s. Here, LB- lower bainite, MA- martensite austenite islands, TM/PM- tempered martensite/prior athermal martensite and RA- retained austenite. The figure on the right is the magnified version of the white box shown in the left figure.



For the condition exactly at  $M_S$  (Iso-245°C) (Figure 3.14), acicular units with carbides aligned parallel inside them are observed and are identified to be lower bainite. Interlath retained austenite can also be identified in between two BF units. The identified lower bainite and retained austenite looks similar to the above  $M_S$  condition along with the vast areas of MA islands (smooth surface after etching). For the condition below  $M_S$  (Figure 3.15), acicular units of lower bainite are found along with the interlath RA structures. At this transformation temperature (200 °C), prior athermal martensite with a volume fraction of 0.21 (Figure 3.9) is formed during the cooling from austenization to this isothermal temperature. This PM gets tempered during the isothermal holding for 5300 seconds along with the formation of BF. Figure 3.15(b) shows a structure with multivariant carbides precipitated inside them. This type of structures with multi variant carbides are not observed in the conditions above or exactly at  $M_S$ . Thus, the structure with multivariant carbides has to be the tempered martensite (TM). These carbides must have precipitated from PM, which was supersaturated with carbon before the start of the isothermal treatment. So, the distinguishing factor between the lower bainite (LB) and tempered martensite (TM) is the way in which the carbides are aligned within the structure <sup>23</sup>.

### 3.5. Micro-hardness Vickers measurements

The micro hardness Vickers for all the conditions is shown in Figure 3.16. The results from the hardness measurement serve as evidence for the microstructural evolution at different isothermal treatments. There seems to be a tendency with the hardness values where it increases with the decrease in the isothermal temperature. It can be observed that there is a significant increase in the hardness value of around 100 HV for the condition Iso-260°C when compared to that of the Iso-300°C. But the phase fractions of these two conditions are very similar to each other (see Figure 3.9), and thus the difference in the hardness value must come from the tempering effect of the bainite <sup>7</sup>. From Figure 3.17 and Figure 3.18, it can be seen that the bainite transformation for the condition Iso-300°C finishes around 2000 seconds and a saturation period (a plateau in the curve) is observed between 2000 seconds and 5300 seconds where bainite does not form. Therefore, the entire volume fraction of bainite gets tempered in the case of Iso-300°C during the saturation period. But in the other conditions, the bainite transformation is not complete at the end of isothermal treatment (the curve keeps increasing even at the end of 5300 seconds). Therefore, the entire volume fraction of bainite does not get tempered in these conditions. This difference in the tempering of bainite is responsible for the huge variation in the hardness values between Iso-300°C and other conditions.

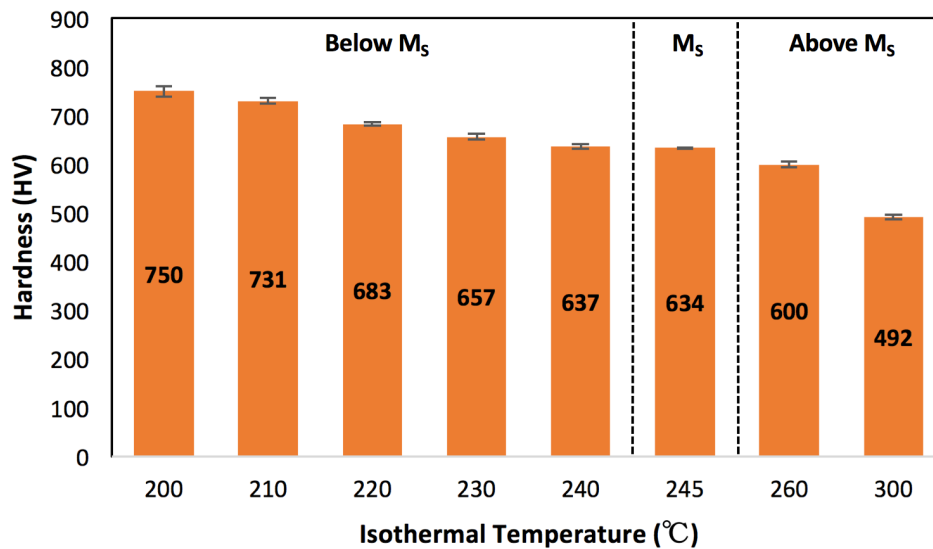


Figure 3.16: The Vickers hardness (HV) measurements for all the isothermal treatments above and below the  $M_S$  temperature with standard deviation error bars.

The increase in the hardness for the conditions Iso-245°C and Iso-240°C when compared to Iso-260°C must be due to the increase in volume fraction of bainite (Figure 3.9). The carbides present in the bainite contributes to this increase in the hardness values. For the isothermal conditions Iso-245°C and Iso-240°C, hardness values do not differ significantly since the phase fractions are similar in those two conditions. The increase in the hardness for the conditions Iso-230°C and Iso-220°C must be associated with the volume fraction of prior athermal martensite and fresh martensite combined and can also be related to the increase in dislocation density of BF with the decrease in transformation temperature<sup>7</sup>. The considerable increase in hardness for conditions Iso-210°C and Iso-200°C must be related to large volume fraction of fresh martensite (0.32 and 0.38 respectively) and prior athermal martensite (0.14 and 0.21 respectively) observed in those two conditions (Figure 3.9). Since the volume fraction of retained austenite does not vary significantly between the conditions, the hardness value is not affected significantly by the volume fraction of RA.

## 3.6. Bainite Transformation Kinetics

### 3.6.1. Analysis with bainite transformation curves

Figure 3.17 (a) and Figure 3.18 (b) represent the evolution of volume fraction of bainite as a function of time for the conditions above and below  $M_S$  respectively, which are obtained through the dilatation data during the isothermal treatment. Figure 3.17 (b) and Figure 3.18 (b) represent the first 1000 seconds of the transformation for the conditions above and below  $M_S$  respectively.

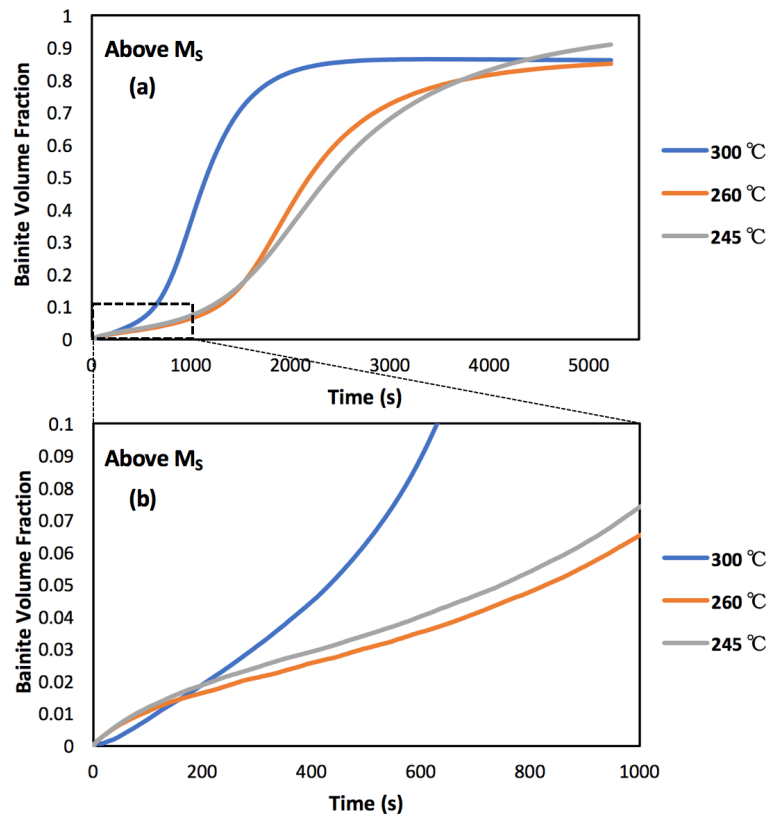


Figure 3.17: (a) Evolution of volume fraction of the bainite as a function of isothermal holding time at different temperatures above and just at  $M_S$  temperature. (b) Magnified plot for the first 1000s of the transformation.

S-shaped curves for the kinetics are observed for all the conditions above and below  $M_S$ . In the case of above  $M_S$  conditions, the curve of Iso-260 °C has shifted to longer times when compared to the condition Iso-300 °C which means that the transformation kinetics is reduced with the decrease in temperature. This is because the diffusion rate decreases with the reduction in the temperature and it is known that the nucleation of bainite involves some diffusion of carbon from the supersaturated bainite plate to the austenite<sup>9,14</sup>. This is also evident from the calculated TTT diagram for the current material where the nose of the TTT lies around the 300 °C mark as seen in Figure 2.4. In the case of Iso-245 °C, there seems to be a slight increase in the kinetics at the beginning of the transformation when comparing to Iso-260 °C (see Figure 3.17(b)). This could probably be because of the possible formation of a small fraction of PM before the start of the isothermal treatment since the treatment is very close to the  $M_S$ .

For the conditions below  $M_S$  (Figure 3.18), the transformation is much faster at the very beginning of the transformation<sup>†</sup> (Figure 3.18(b)) when comparing to that of the above  $M_S$  conditions (Figure 3.17(b)). The acceleration increases with the decrease in the isothermal

<sup>†</sup> Note: There is a small bump or dip (denoted by arrows) seen in the beginning of the bainite transformation (Magnified image in Figure 3.18(b)) and this is due to the start of vacuum in the dilatometry at the start of isothermal treatment after the initial quench. The proof for this is shown in the Appendix 7.3.

temperature, and this can be correlated with the increase in the volume fraction of PM. The acceleration is observed only at the very beginning of the transformation after which the curves follow an S-shaped behaviour.

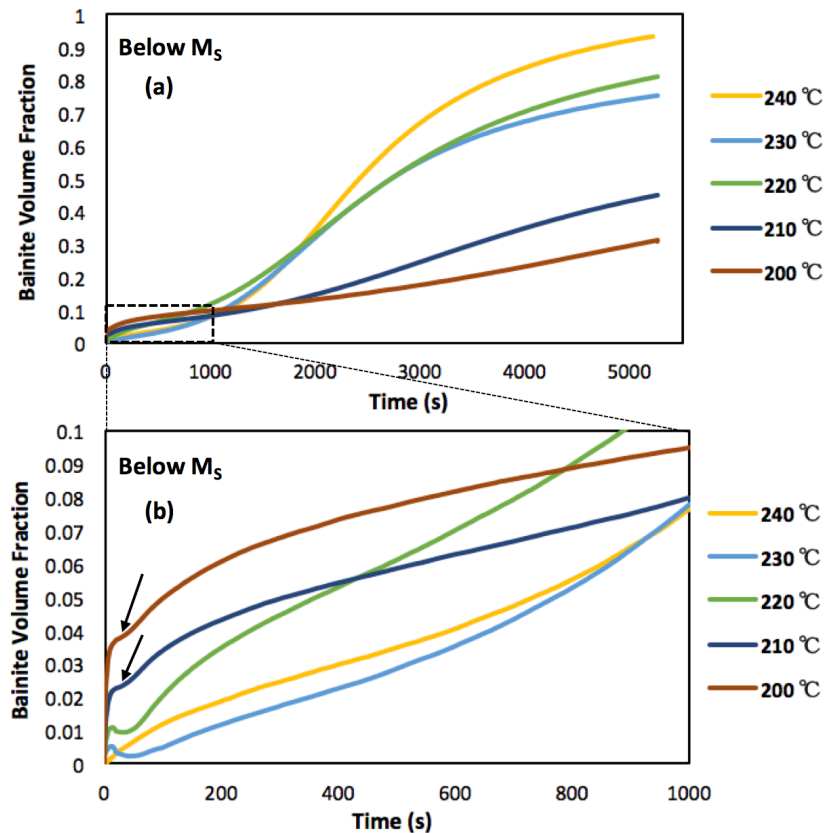


Figure 3.18: (a) Evolution of volume fraction of the bainite as a function of isothermal holding time at different temperatures below  $M_S$  temperature. (b) Magnified plot for the first 1000s of the transformation.

To quantify this acceleration effect, Figure 3.19 shows the evolution of volume fraction of bainite as a function of time for three different conditions: Iso-260 °C (above  $M_S$ ), Iso-210 °C (below  $M_S$ ) and Iso-200 °C (below  $M_S$ ). Figure 3.19(b) shows the first 1000 seconds of the transformation. The volume fraction of the bainite at two different times (200 s and 400 s) since the beginning of the isothermal transformation is given in Table 3.1, which shows the formation of higher volume fraction of bainite for the below  $M_S$  conditions when compared to the above  $M_S$  condition. This shows that there is acceleration in the bainite transformation kinetics due to the presence of PM depending upon the volume fraction of PM formed before the start of the isothermal treatment.

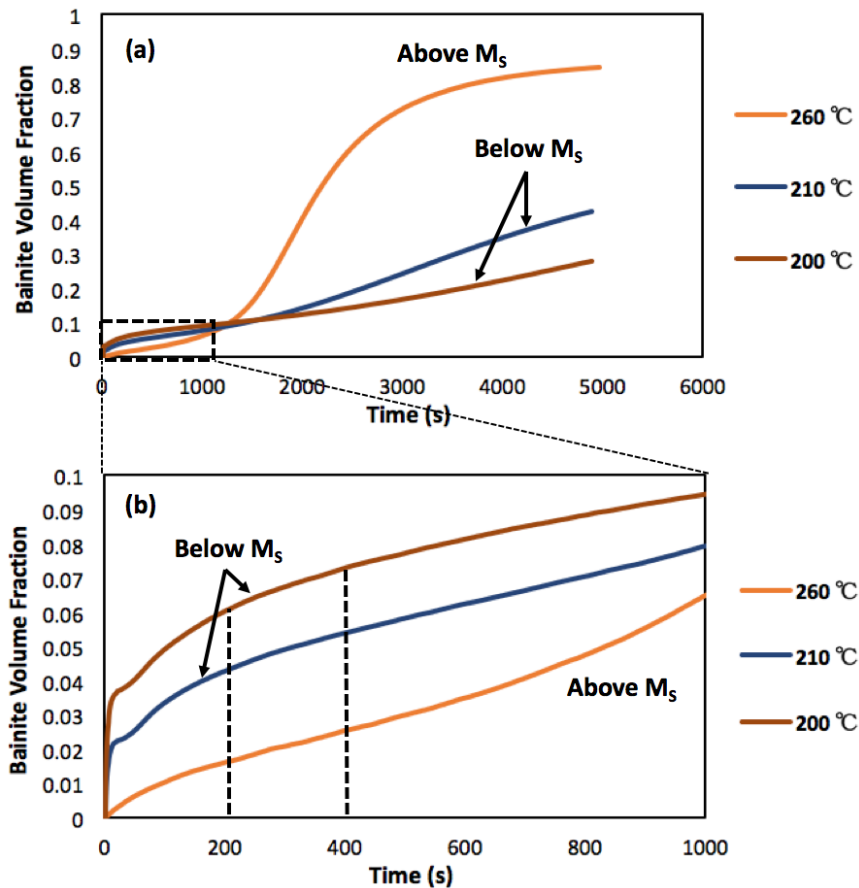


Figure 3.19: (a) Bainite fraction as a function of time at 260 °C, 210 °C and 200 °C- Above and below the  $M_S$  temperature. (b) Magnified plot for the first 1000s of the transformation.

Table 3.1: Comparison of the bainite volume fraction at two different times (200s and 400s) for three temperatures 260 (above  $M_S$ ), 210 and 200 (below  $M_S$ ).

T (°C) \ t (s)	200 s	400 s
260 °C	0.01	0.02
210 °C	0.04	0.05
200 °C	0.06	0.07

For the conditions below  $M_S$  (Figure 3.18), the decrease in the isothermal temperature causes the acceleration of the transformation kinetics of bainite to increase. On the other hand, the decrease in the isothermal temperature below  $M_S$  causes the final volume fraction of bainite to decrease. This shows that there is a trade off between the final volume fraction of bainite, volume fraction of unstable austenite and the transformation kinetics, based on the isothermal temperature below  $M_S$ . Thus the final volume fraction of bainite and the bainite transformation kinetics below  $M_S$  depends on the isothermal temperature.

### 3.6.2. Analysis with nucleation rate

As mentioned earlier, in order to determine the effect of carbon content on the transformation kinetics of bainite along with the effect of PM, the present study will be compared to the research of A. Navarro-López et al. <sup>1</sup> Therefore, the analysis of the kinetics of

bainite transformation in this current study will be similar to the method used by A. Navarro-López et al.<sup>1</sup> for the purpose of comparison.

Nucleation rate and the density of potential nucleation sites will be used to quantitatively determine effect of PM on the kinetics of bainite transformation<sup>1</sup>. The change in volume fraction bainite ( $f^B$ ) with time ( $t$ ) can be described by<sup>57</sup>.

$$\frac{df^B}{dt} = \frac{dN}{dt} \times V_u \quad [10]$$

where,  $dN/dt$  is the nucleation rate per unit volume and  $V_u$  is the volume of a bainite subunit.

### **Determination of volume of bainite subunit**

The volume of the bainite subunits could be obtained by two methods proposed in the literature and they are as follows:

- 1.) The volume of the bainite subunits is assumed to be constant with temperature sometimes in the literature. The volume assumed is  $0.2 \times 10 \times 10 \mu\text{m}^3$  according to<sup>58</sup>. Here, the dimension  $0.2 \mu\text{m}$  represents the thickness of the bainite subunit.
- 2.) Parker<sup>59</sup> modelled a temperature dependent empirical equation for the thickness of the bainite subunit based on the experimental data from Chang and Bhadeshia<sup>60</sup>. Matsuda and Bhadeshia<sup>58</sup> assumed that all the dimensions scale with the temperature and used the empirical formula from Parker<sup>59</sup> to find the volume of the bainite subunit (Equation 11). However, this empirical equation is only valid between the temperature range of  $250 \text{ }^\circ\text{C}$ -  $500 \text{ }^\circ\text{C}$  ( $523 \text{ K}$ -  $773 \text{ K}$ ).

$$V_u = 2.0 \times 10^{-17} \times \left( \frac{T-528 \text{ K}}{150 \text{ K}} \right)^3 \text{ m}^3 \quad [11]$$

Equation 11 cannot be used in the current study since most of the isothermal temperatures employed in the present study is out of the temperature range valid for the Equation 11. Also, a constant value for the volume of bainite subunit cannot be assumed since it is not the real case. This is because, refinement of the microstructure is known to be present when the transformation temperature is reduced<sup>58</sup>. It has been reported that factors such as driving force, austenite strength and transformation temperatures affect the volume of the bainite units<sup>61</sup>.

L.C. Chang<sup>62</sup> reported that the thickness of the bainite subunit decreases with decreasing transformation temperature and starts saturating below the  $300 \text{ }^\circ\text{C}$  mark. It has to be noted that a small reduction in the thickness values is still observed for the transformation temperatures below  $300 \text{ }^\circ\text{C}$ <sup>62</sup>. The decrease in the thickness is much more pronounced than the decrease in the other two dimensions and, therefore the other two dimensions will be



assumed to be constant in the current research. Thus, it can be assumed that the volume of the bainite subunit decreases three-dimensionally until 300 °C and decreases one dimensionally (only thickness) below 300 °C as shown in Figure 3.20.

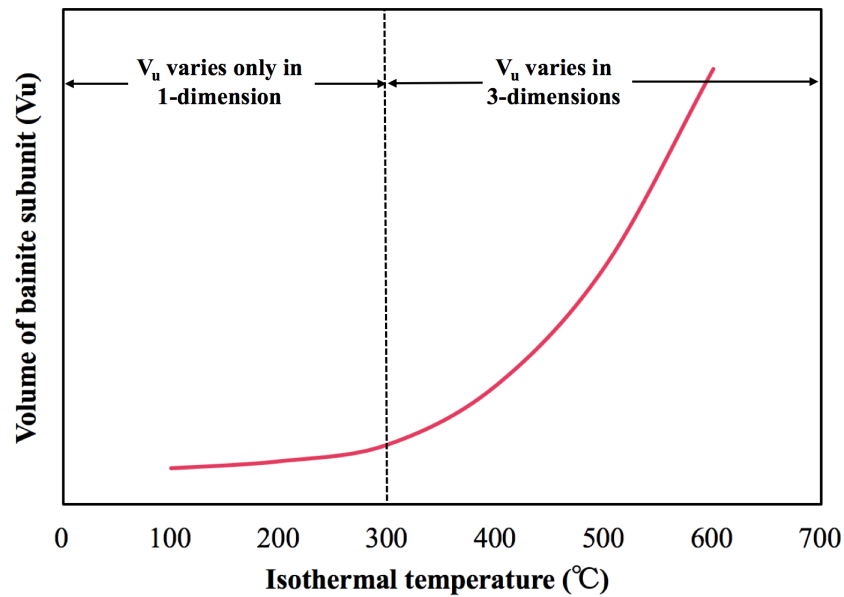


Figure 3.20: Variation of volume of bainite subunit as a function of isothermal temperature.

Yanbing Guo et al.<sup>63</sup> reported a decrease in the thickness of the bainite subunits with decreasing isothermal temperature below the 300 °C mark. The thickness of the bainite subunits was reported for the isothermal temperatures 300 °C, 250 °C and 200 °C. The thickness data from Yanbing Guo et al.<sup>63</sup> has been interpolated and used in the current study. It has to be noted that the other two dimensions are kept constant (10 μm and 10 μm respectively) since no proper literature is found for the other two dimensions. The dimensions and the calculated volume of the bainite subunits are presented in Table 3.2.

Table 3.2: Calculation of volume of bainite subunit with varying thickness values based on<sup>62</sup> and<sup>63</sup>.

Isothermal Condition (°C)	Thickness (μm)	Length (μm)	Width (μm)	Volume of bainite subunit $V_u$ (m <sup>3</sup> )
300	0.0696	10	10	6.955 E-18
260	0.0585	10	10	5.845 E-18
245 (M <sub>s</sub> )	0.0547	10	10	5.470 E-18
240	0.0535	10	10	5.350 E-18
230	0.0512	10	10	5.117 E-18
220	0.0490	10	10	4.895 E-18
210	0.0468	10	10	4.682 E-18
200	0.0448	10	10	4.480 E-18

Based on the nucleation rates calculated from the Equation 10 and using the data from Figure 3.17 and Figure 3.18, the evolution of the nucleation rates as a function of volume fraction of bainite is plotted in Figure 3.21 and Figure 3.22 for the conditions above and below

$M_S$ . To observe the nucleation rate at the very beginning of the transformation, the transformation of the first 0.1 volume fraction of the bainite is shown in Figure 3.21 (b) and Figure 3.22 (b). In the case of above  $M_S$  condition (Iso-260°C) and exactly at  $M_S$  condition (Iso-245°C), the nucleation rate reaches the maximum at the beginning of the transformation and then gets to the minimum very soon around 0.03 volume fraction of the bainite. Afterwards, it starts to increase, reaching a peak at around 0.6 volume fraction of bainite. This second peak which is found around 0.6 volume fraction of bainite corresponds well with the inflection points of the curves from Figure 3.17 (a). The maximum, which is seen at the beginning of the transformation, must be due to the nucleation at the  $\gamma$ - $\gamma$  interfaces which gives an acceleration at the start of the transformation and then fades off when the potential nucleation sites in the  $\gamma$ - $\gamma$  interface are reduced (since they are consumed already). The nucleation rates after the second peak start to decrease till the end of the isothermal treatment.

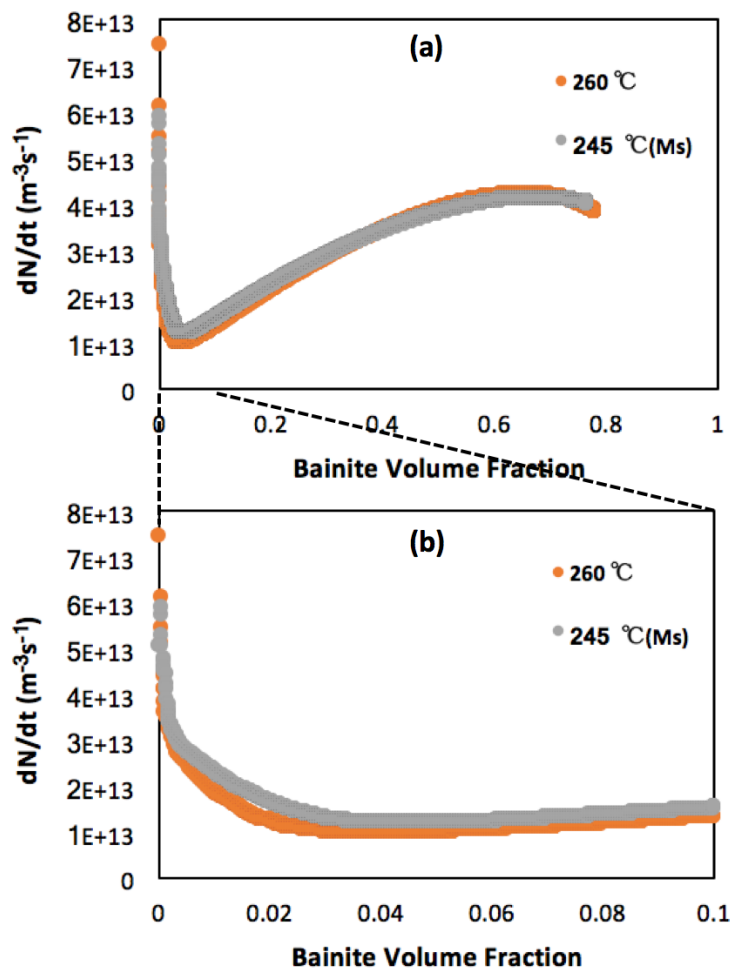


Figure 3.21: Variation of nucleation rates at different isothermal temperatures above and just at  $M_S$  temperature.

In the case of below  $M_S$  conditions (Iso-210°C and Iso-200°C) (Figure 3.22), there is a maximum obtained at the beginning of the transformation similar to conditions above  $M_S$ . But the magnitude is much higher below  $M_S$  (in the order of  $10^{15}$ ) when compared to the above  $M_S$  (in the order of  $10^{13}$ ). Then after, the nucleation rates decrease rapidly till the end of the isothermal treatment. It is known that the decrease in the isothermal temperature gives rise to

smaller units of bainite, and the presence of PM creates new potential nucleation sites (from  $\alpha'$ - $\gamma$  interfaces) for the bainite transformation. Based on this, the nucleation rates for the conditions below  $M_S$  must be much faster than the conditions above  $M_S$ . This effect can be seen from the Figure 3.22(b) confirming the phenomenon mentioned above.

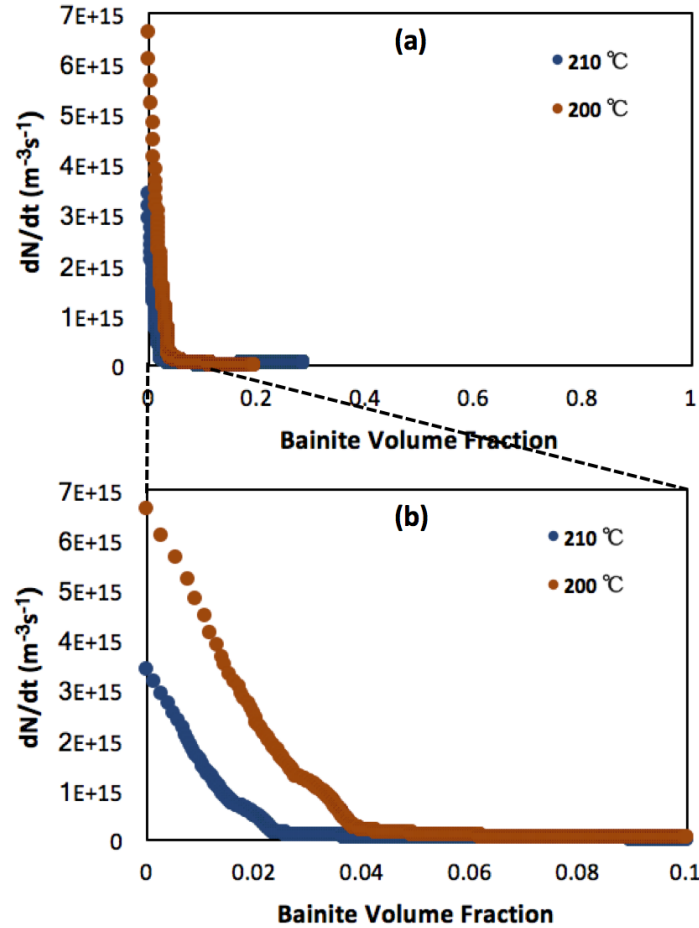


Figure 3.22: Variation of nucleation rates at different isothermal temperatures below the  $M_S$  temperature.

Table 3.3: Various parameters (experimental and theoretical) obtained for the different isothermal temperatures above, just and below  $M_S$  temperature.  $V_u$  (Volume of subunits of bainite),  $f^{PM}$  (Volume fraction of PM),  $t_i$  (Time elapsed since the beginning of isothermal treatment),  $(dN/dt)_{0.5}$  (Nucleation rate at  $t_i=0.5$  s),  $n_{sites}$  (Number of nuclei formed per second at  $t_i$ ) and  $f^{fB}$  (Experimental volume fraction of bainitic ferrite formed after  $t_i$ ).

Isothermal Temperature (°C)	$V_u$ ( $m^3$ )	$f^{PM}$	$t_i$ (s)	$(dN/dt)_{0.5}$ ( $m^{-3}s^{-1}$ )	$(n_{sites})_{0.5}$ ( $s^{-1}$ )	$(f^{fB})_{0.5}$
300	6.95 E-18	0	0.5	2.61 E+13	3.03E-02	2.26E-04
260	5.84 E-18	0	0.5	6.23 E+13	7.22E-02	5.80E-04
245 ( $M_S$ )	5.47 E-18	0	0.5	5.89 E+13	6.82E-02	6.69E-04
240	5.35 E-18	0.003	0.5	4.95 E+14	5.73E-01	4.24E-04
230	5.11 E-18	0.026	0.5	2.10 E+15	2.434	2.74E-03
220	4.89 E-18	0.070	0.5	1.20 E+15	1.392	3.17E-03
210	4.68 E-18	0.139	0.5	3.13 E+15	3.626	7.22E-03
200	4.48 E-18	0.214	0.5	6.08 E+15	7.041	1.44E-02

The volume of bainite subunits ( $V_u$ ) calculated from the theoretical data and the initial nucleation rate  $(dN/dt)_{0.5}$  calculated from the experimental data are presented in Table 3.3 for all the isothermal conditions. The initial nucleation rate presented here is at an elapsed time of 0.5 seconds from the beginning of the transformation. This elapsed time of 0.5 seconds has been selected to present the effect of PM alone on the bainite transformation kinetics by avoiding the autocatalytic effect<sup>1</sup>.

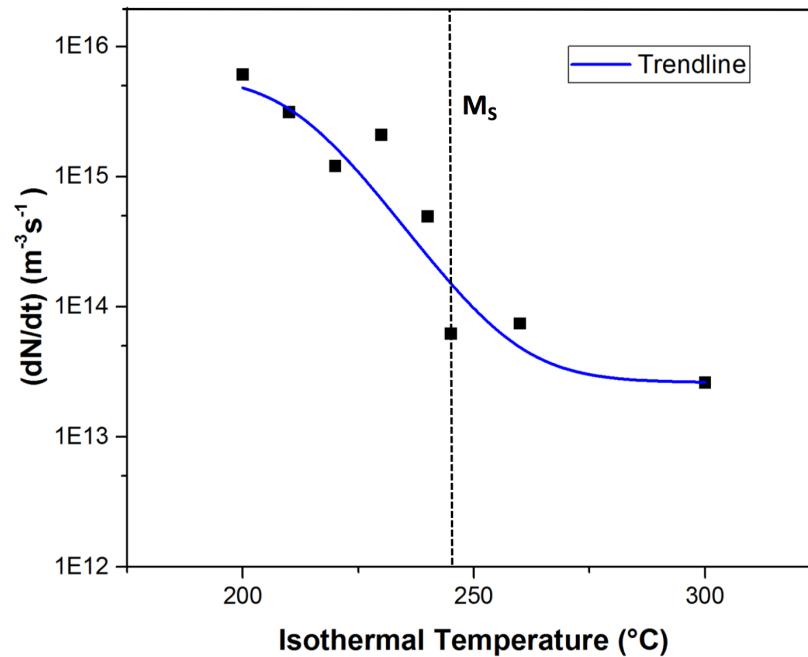


Figure 3.23: The summary of the initial nucleation rates (at 0.5 seconds from the start of isothermal temperature) for all the conditions above, just and below the  $M_S$  temperature (isothermal temperature is in the  $x$ -axis).

The initial nucleation rates  $(dN/dt)_{0.5}$  for all the conditions is shown in Figure 3.23 with a logarithmic plot. It can be observed that the nucleation rates increase rapidly from the above  $M_S$  conditions to the below  $M_S$  conditions. The significant increase in the initial nucleation rate can be related to the presence of PM for the conditions below  $M_S$ . Thus the differences seen in the nucleation rates and the evolution of volume fraction of bainite above and below  $M_S$  (as shown in Figure 3.19, Figure 3.21 and Figure 3.22) are now confirmed by Figure 3.23.

### 3.6.3. Analysis based on the $n_{sites}$

The nucleation rate of the bainite at the beginning of the transformation is seen to increase with the increase in the volume fraction of PM. This implies that the volume fraction of bainite will also increase at the beginning of the transformation. The increase in the kinetics of bainite transformation can be defined by deriving a relationship between the volume fraction of PM, the volume fraction of LB and the interfaces involved in the transformation<sup>1</sup>. In order to counter this, a variable has been introduced, which is  $n_{sites}$ <sup>1</sup>. It is the representation of the number of nucleation events per second in the austenite grain. The  $n_{sites}$  at the beginning of the isothermal transformation has been calculated using the Equation 12<sup>1</sup> and is given in Table 3.3 for all the conditions.

$$n_{sites}(t_i) = \left(\frac{dN}{dt}\right)_{t_i} \times V_{grain}^{\gamma} \quad [12]$$

where,  $V_{grain}^{\gamma}$  is the average volume of an austenite grain. Thermal etching has been used to determine the average diameter of the austenite grain which is  $\sim 10.5 \mu\text{m}$ .

In the case of above  $M_S$  conditions, the only source of potential nucleation sites at the beginning of the transformation is the  $\gamma$ - $\gamma$  interfaces. But in the case of below  $M_S$  conditions, the presence of  $\alpha'$ - $\gamma$  interfaces together with the  $\gamma$ - $\gamma$  interfaces provides more potential nucleation sites at the beginning of the transformation. It has been assumed that there is no effect from the bainite- austenite ( $\alpha^b$ - $\gamma$ ) interfaces at the beginning of the isothermal transformation. The  $n_{sites}$  value increases for below  $M_S$  conditions when compared to above  $M_S$  conditions and this can be related to two possible reasons. One is the creation of  $\alpha'$ - $\gamma$  interfaces due to the presence of PM, and the other is the existence of temperature difference which creates the additional driving force when the isothermal temperature is decreased. The difference between the values of the  $n_{sites}$  just above and just below  $M_S$  is around 1 order of magnitude. Both the temperature difference and the  $\alpha'$ - $\gamma$  interfaces play an important role on the transformation kinetics. But the effect due to the increase in the density of the potential nucleation sites (from  $\alpha'$ - $\gamma$  interfaces) has a substantial impact on the nucleation rates at the beginning of the transformation below  $M_S$  when compared to the effect due to the temperature difference. It also has to be noted that the acceleration effect is observed only at the beginning of the transformation and fades off after the formation of a very small volume fraction of bainite. For instance, in the condition Iso-200°C, the acceleration saturates after the formation of 0.04 volume fraction of bainite. Discussion on this effect will be presented in Section 3.7.

#### 3.6.4. Effect of $\alpha'$ - $\gamma$ interfacial area

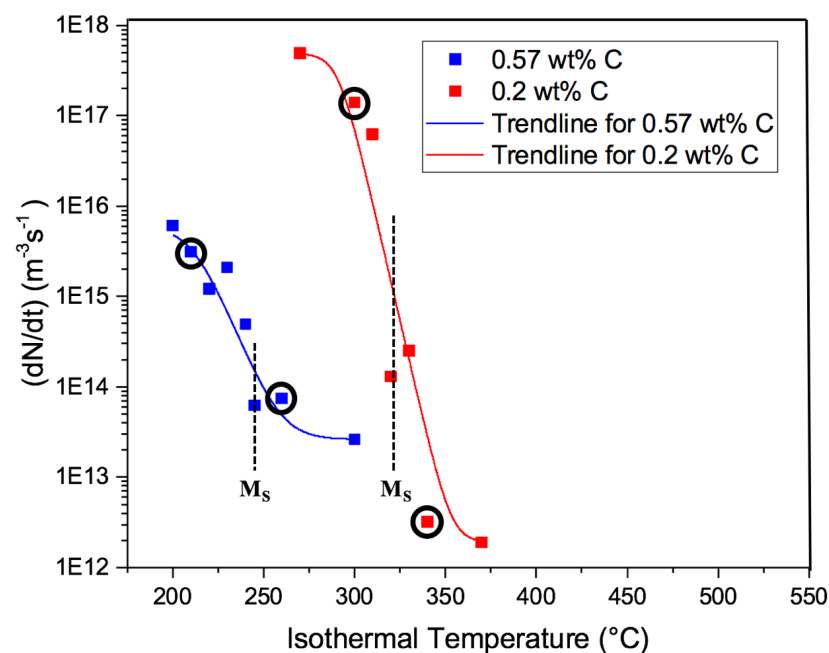
Similar to the results of A. Navarro-López et al.<sup>1</sup>, there is no proportional relationship between the increase in  $n_{sites}$  and the increase in the volume fraction of the PM. This is also seen with the relationship between the volume fraction of PM and the volume fraction of BF since they do not increase proportionally. The reason for this was mentioned by A. Navarro-López et al.<sup>1</sup> that the subunits of the bainitic ferrite nucleates in the  $\alpha'$ - $\gamma$  interfaces and hence the nucleation process will depend upon the area of  $\alpha'$ - $\gamma$  interfaces and not on the volume fraction of the PM. Thus the way the martensite laths are arranged in the microstructure plays an important role on the nucleation rates. Usually, the martensite units are formed in clusters rather than forming as individual units which are homogeneously distributed in the microstructure<sup>1</sup>. This is the reason due to which the  $n_{sites}$  does not increase proportionally with the fraction of prior athermal martensite. It is thus clear that the area of  $\alpha'$ - $\gamma$  interface serves as an important aspect for the transformation kinetics for the conditions below  $M_S$  temperature. But, a further study regarding this is needed to derive a better understanding of this relationship.

### 3.7. Effect of Carbon Content on the Transformation Kinetics of Bainite along with the presence of Prior athermal Martensite

As mentioned earlier, the work of A. Navarro-López et al. <sup>1</sup> (low carbon steel: 0.2C-3.51Mn-1.52Si-0.25Mo-0.04Al in wt%) will be compared to the results of the current work (medium carbon steel) to study and compare the behaviour of bainite transformation kinetics with varying carbon content. Given the fact that the alloy composition is slightly different for the low carbon steel than the material in this study, it is worth to compare the effect of carbon content on the kinetics of bainite transformation due to the presence of PM. There are two important observations from the assessment, and they are discussed below:

#### 1. Initial nucleation rate ( $dN/dt$ at 0.5 seconds):

Figure 3.24 shows the comparison of the initial nucleation rates (at 0.5 seconds) for the low carbon steel (red curve) and medium carbon steel (blue curve) along with their respective tables denoting the difference in the  $(dN/dt)_{0.5}$  between conditions above and below  $M_S$ .



Low carbon steel	$f^{PM}$	$(dN/dt)_{0.5} (m^{-3}s^{-1})$
Below $M_S$	0.16	$\sim 10^{17}$
Above $M_S$	0	$\sim 10^{12}$
Difference in $(dN/dt)_{0.5}$		$\sim 10^5$

Medium carbon steel	$f^{PM}$	$(dN/dt)_{0.5} (m^{-3}s^{-1})$
Below $M_S$	0.14	$\sim 10^{15}$
Above $M_S$	0	$\sim 10^{13}$
Difference in $(dN/dt)_{0.5}$		$\sim 10^2$

Figure 3.24: Comparison of the initial nucleation rates for low carbon steel <sup>1</sup> (red curve) and medium carbon steel (blue curve) for the condition below  $M_S$  having a similar fraction PM. The black circles denote the conditions which are considered for the comparison. The tables represent the difference between the initial nucleation rate for above and below  $M_S$  conditions for the low carbon steel (left table) and medium carbon steel (right table).

It is evident that the acceleration below  $M_S$  is quite high for the low carbon steel where the difference in the nucleation rate between the above and below  $M_S$  conditions is observed to

be  $10^5$  orders of magnitude. The selected condition below  $M_S$  has a volume fraction of PM of 0.16. Whereas in the case of medium carbon steel, the difference in the  $(dN/dt)_{0.5}$  between the conditions above and below  $M_S$  is seen to be 2 orders of magnitude. The condition selected below  $M_S$  for the medium carbon steel has a volume fraction of PM of 0.14, which is quite similar to the condition selected in the low carbon steel below  $M_S$ .

Thus it is quite clear that the difference in the initial nucleation rates between the conditions above  $M_S$  and below  $M_S$  is significantly higher for the low carbon steel when compared to the medium carbon steel. The reason for such behaviour could be explained as follows:

**a.) Volume of bainite subunit ( $V_u$ ):**

The theoretical dimensions which are used in the current study (0.57 wt% C) to calculate the volume of the bainite subunit have an assumption that the two other dimensions except for the thickness of the bainite are constant for all the isothermal treatments (10  $\mu\text{m}$  and 10  $\mu\text{m}$  respectively) due to certain limitations. This might not be the actual case since the microstructure will tend to refine when the transformation temperature is reduced<sup>61</sup>. This could have resulted in an over estimation of the volume of bainite subunits. When the volume of the bainite subunits is larger, then it means that the grain boundary surface area per unit volume becomes smaller and vice versa. Thus the overestimation of the volume of bainite subunit could have resulted in an underestimation of the nucleation rate in the case of medium carbon steel (current study).

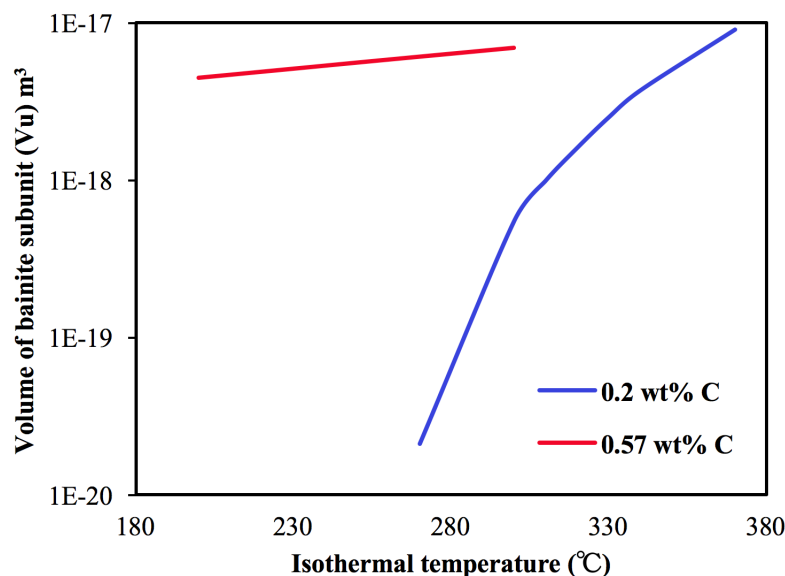


Figure 3.25: Logarithmic plot of the variation of the volume of bainite subunit as a function of isothermal temperature in the current study (0.57 wt% C) and in the research of A. Navarro-López (0.2 wt% C).

In the research of A. Navarro-López et al.<sup>1</sup> (0.2 wt% C), the volume of bainite subunit for all the isothermal conditions was calculated using the empirical equation from Matsuda and Bhadeshia<sup>58</sup> (Equation 11). Usage of Equation 11 was possible since the isothermal temperatures were within the range of the temperature (250 °C- 500 °C) valid for Equation 11.



The variation of the volume of bainite subunit as a function of isothermal temperature in the current study and the research of A. Navarro-López et al.<sup>1</sup> are compared in Figure 3.25. It is clear that the variation of the volume of bainite subunit with the decrease in isothermal temperature is small in the current study (0.57 wt% C) when compared to the work of A. Navarro-López et al.<sup>1</sup> (0.2 wt% C).

**b.) Carbon content:**

The other reason could be related to the carbon content of the steel where the increase in carbon content retards the kinetics of bainite formation<sup>27</sup>. This is because, the increase in carbon content decreases the driving force for the bainite transformation. It is well known that the thermal stability of the retained austenite increases with the increase in the average carbon content<sup>64,65</sup> which means that the transformation of bainite becomes relatively difficult with the increase in carbon content, and so is the decrease in the nucleation rate.

It can be observed that the Si content is different between the current study (0.006 wt%) and the study of A. Navarro-López et al.<sup>1</sup> (1.52 wt%). This difference in the Si content could have influenced the transformation kinetics to some extent. Since the effect of Si on the transformation kinetics of bainite is unclear from the literature, further investigation regarding the same is required to concrete this effect.

**2. Duration of the acceleration effect:**

Another interesting observation is the duration of the acceleration effect due to the PM. The duration here is represented in terms of volume fraction of bainite formed. The comparison between the duration of the acceleration effect for the low carbon steel and medium carbon steel is presented in Figure 3.26, where one condition below  $M_S$  has been selected for both steels, and they are marked by red boxes in the figure. These two conditions have been chosen for the comparison since they have a similar volume fraction of PM (0.16 in the case of low carbon steel and 0.14 in the case of medium carbon steel).

According to Figure 3.26, the duration of the accelerating effect for the low carbon steel is quite longer than that of the medium carbon steel. The effect stops at ~0.2 volume fraction of bainite for the low carbon steel and at ~0.02 volume fraction of bainite for the medium carbon steel (note that the x-axis scale is different for the two plots). The reason for this must be the effect due to the carbon content as mentioned above.



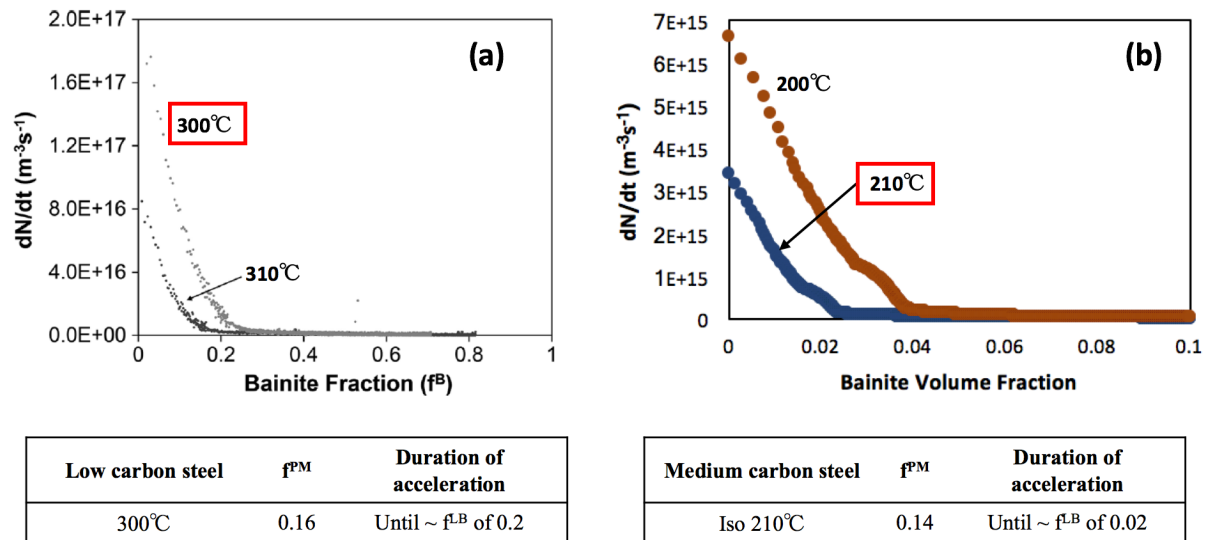


Figure 3.26: Comparison of the duration of the acceleration effect seen in (a) low carbon steel and (b) medium carbon steel. The red box indicates the condition which is considered for the comparison. Note that the x-axis scale is different in (a) and (b).

For the above explained two observations, there could be a possible competition between the deceleration effect due to the higher carbon content and the acceleration effect due to the presence of PM at the beginning of the transformation for the medium carbon steel. Thus, the decrease in carbon content or an increase in the interfacial area of  $\alpha'$ - $\gamma$  interface could increase the bainite transformation kinetics and vice versa.

The acceleration due to the presence of PM (by the creation of potential nucleation sites through  $\alpha'$ - $\gamma$  interfaces) is observed in both the low carbon and medium carbon steels, but the acceleration is much weaker in the medium carbon steel than the low carbon steel based on both intensity and the duration of the acceleration. This could be mainly attributed to the carbon content of the steel and the calculated volume of the bainite subunits.

# 4. Conclusions

The effect of the prior athermal martensite (PM) and the carbon content on the bainite transformation kinetics have been studied by comparing the isothermal treatments above and below  $M_S$  in a medium carbon manganese steel. The main conclusions obtained are as follows:

## Results based on the experimental work from current study:

1. The isothermal product formed below  $M_S$  has been identified as lower bainite, where the prior athermal martensite had already formed before the start of the isothermal treatment. The morphological characteristics of the lower bainite formed below  $M_S$  are found to be similar to those of the lower bainite formed in conditions above  $M_S$  and exactly at  $M_S$ . The formation of MA islands was found to be because of the heterogeneous distribution of Mn in the material.
2. The bainite transformation kinetics is accelerated by the presence of prior athermal martensite due to the large amounts of potential nucleation sites created from the austenite-martensite ( $\gamma$ - $\alpha'$ ) interfaces. The interfacial area of the austenite-martensite ( $\gamma$ - $\alpha'$ ) interfaces has a significant impact on the nucleation process rather than the volume fraction of PM.
3. The initial nucleation rate at the beginning of the isothermal transformation for the conditions below  $M_S$  increases by two orders of magnitude when compared to the conditions above  $M_S$  which do not have any PM.
4. The final volume fraction of bainite and the acceleration of bainite transformation kinetics for the conditions below  $M_S$  depends on the transformation temperature.

## Results based on the comparison of steels with different carbon contents:

5. The acceleration in the kinetics of bainite transformation is much weaker in the case of medium carbon steel (0.57 wt% C) when compared to the low carbon steel (0.2 wt% C).
6. Competition between the effect due to the carbon content and the effect due to the presence of PM on the bainite transformation kinetics is observed at the beginning of the transformation for the conditions below  $M_S$ . This means that the carbon content and the presence of PM have a significant role on the intensity and duration of the acceleration at the start of the transformation.

# 5. Recommendations

The following aspects are recommended to be studied during the future work on a similar field of study:

1. The volume of the bainite subunits for the lower isothermal temperatures could be quantified by measuring the dimensions of the bainite plate using TEM. This could be beneficial to study the nucleation rates more precisely and to compare it with the isothermal treatments at higher temperatures.
2. A better quantitative relationship between the  $\alpha'$ - $\gamma$  interfacial area and the transformation kinetics could be derived to understand the effect more clearly.
3. The mechanism responsible for the acceleration due to the presence of PM remains unclear. The two mechanisms which have been reported are: 1.) The  $\alpha'$ - $\gamma$  interfacial area serving additional potential nucleation sites and 2.) The strain introduced due to the presence of PM in the austenite matrix. A study on the actual effect which is responsible for the acceleration could answer this research question.
4. A high carbon steel shall be studied to see if the effect due to the carbon content on the transformation kinetics of bainite is consistent along with the effect due to the presence of PM.
5. The effect of the Si content on the transformation kinetics of the bainite is unclear from the literature. Thus it could be interesting to study the effect of Si by comparing two steels with varying Si contents.

# 6. References

1. Navarro-López, A., Sietsma, J. & Santofimia, M. . Effect of Prior Athermal Martensite on the Isothermal Transformation Kinetics Below  $M_s$  in a Low-C. *Metall. Mater. Trans. A* **47A**, 1028–1039 (2016).
2. Porter, D. . & Easterling, K. . No Title. in *Phase transformations in metals and alloys* (1992).
3. Christian, J. W. No Title. in *Theory of Transformations in Metals and Alloys* (Oxford, 2002).
4. Honeycombe, R. W. . & Bhadeshia, H. K. D. . *Steels- Microstructure and Properties. Iron Steel Institute, London* (1995).
5. Hehemann, R. ., Kinsman, K. . & Aaronson, H. . A debate on the bainite reaction. *Metall. Mater. Trans.* **3**, 1077–1094 (1972).
6. Aaronson, H. . & Lee, H. . Another visit to the three definitions of bainite. *Scr. Metall.* **21**, 1011 (1987).
7. Bhadeshia, H. K. D. . *Bainite in steels. The Institute of Materials* (2001).
8. Reynolds, W. ., Aaronson, H. . & Spanos, G. A summary of the present diffusionist views on bainite. *Mat. Trans. JIM* **32**, 737–746 (1991).
9. Ohmori, Y. & Maki, T. Bainitic transformation in view of displacive mechanism. *Mat. Trans. JIM* **32**, 631–641 (1991).
10. Nishiyama, Z. *Martensitic Transformations. Acad. Press* (1978).
11. Roberts, C. . Effect of carbon on the volume fractions and lattice parameters of retained austenite and martensite. *Trans. AIME* **197.2**, 203–204 (1953).
12. Krauss, G. Deformation and Fracture in Martensitic Carbon Steels Tempered at Low Temperatures. *ASM Int.* **32**, (2001).
13. Kozeschnik, E. & Bhadeshia, H. K. D. H. Influence of silicon on cementite precipitation in steels. *Inst. Mater. Miner. Min.* **24**, 343–347 (2008).
14. Olson, G. ., Bhadeshia, H. K. D. . & Cohen, M. Coupled diffusional/displacive transformations. *Acta Metall.* **37.2**, 381–390 (1989).
15. Sandvik, B. P. . The bainite reaction in Fe-Si-C alloys: the secondary stage. *Metall. Mater. Trans. A* **13A**, 789–800 (1982).
16. Takahashi, M. & Bhadeshia, H. K. D. . Model for transition from upper to lower bainite. *Mater. Sci. Technol* **6**, 592–603 (1990).
17. Pickering, F. . Transformations and Hardenability in Steels. *Ann Arbor, MI* 109–129 (1967).
18. Bohemen, S. M. C. Van, Santofimia, M. J. & Sietsma, J. Experimental evidence for bainite formation below  $M_s$  in Fe – 0 . 66C. **58**, 488–491 (2008).
19. Kolmskog, P., Borgenstam, A., Hillert, M., Babu, S. S. & Hedstro, P. Direct Observation that Bainite can Grow Below  $M_s$ . *Miner. Met. Mater. Soc. ASM Int.* (2012).
20. Kim, D., Speer, J. . & Cooman, B. C. De. The Isothermal Transformation of Low-Alloy Low-C CMnSi Steels below  $M_s$ . *Mater. Sci. Forum* **654–656**, 98–101 (2010).
21. Kim, D., Speer, J. G. & Cooman, B. C. D. E. Isothermal Transformation of a CMnSi Steel Below the  $M_s$  Temperature. *Metall. Mater. Trans. A* **42**, 1575–1585 (2011).
22. Kim, D., Lee, S. & Cooman, B. C. D. E. Microstructure of Low C Steel Isothermally Transformed in the  $M_s$  to  $M_f$  Temperature Range. *Miner. Met. Mater. Soc. ASM Int.*

- 43**, (2012).
23. Navarro-López, A., Hidalgo, J., Sietsma, J. & Santofimia, M. . Characterization of Bainitic/Martensitic Structures formed in Isothermal Treatments Below the Ms Temperature. (2015).
  24. Sourmail, T. & Smanio, V. Low temperature kinetics of bainite formation in high carbon steels. *Acta Mater* **61**, 2639–2648 (2013).
  25. Toji, Y., Matsuda, H. & Raabe, D. Effect of Si on the acceleration of bainite transformation by pre- existing martensite. *Acta Mater.* **116**, 250–262 (2016).
  26. Santofimia, M. ., Zhao, L. & Sietsma, J. Microstructural evolution of a low-carbon steel during application of quenching and partitioning heat treatments after partial austenitization. *Met. Mater. Trans. A* **40.1**, 46 (2009).
  27. Zhu, K., Chen, H., Masse, J., Bouaziz, O. & Gachet, G. The effect of prior ferrite formation on bainite and martensite transformation kinetics in advanced high-strength steels. *Acta Mater.* **61**, 6025–6036 (2013).
  28. Ravari, B. K. & Ahmadabadi, M. N. Influence of Alloying Elements on the Bainitic Transformation of Ductile Iron. *Trans Tech Publ.* **457**, 175–180 (2011).
  29. Yang, Z. & Fang, H. An overview on bainite formation in steels. *Solid State Mater Sci* **9.6**, 277–286 (2005).
  30. Marder, A. & Krauss, G. The morphology of martensite in iron-carbon alloys. *ASM Trans Quart* **60.4**, 651–660 (1967).
  31. Krauss, G. Deformation and fracture in martensitic carbon steels tempered at low temperatures. *Met. Mater Trans B* **32.4**, 861–877 (2001).
  32. Gong, W., Tomota, Y., Harjo, S., Su, Y. H. & Aizawa, K. Effect of prior martensite on bainite transformation in nanobainite steel. *Acta Mater.* **85**, 243–249 (2015).
  33. Smanio, V. & Sourmail, T. Effect of partial martensite transformation on bainite reaction kinetics in different 1% C steels. *Solid State Phenom* **172**, 821–826 (2011).
  34. Kawata, H., Hayashi, K., Sugiura, N., Yoshinaga, N. & Takahashi, M. Effect of Martensite in Initial Structure on Bainite Transformation. *Mater. Sci. Forum* 3307–3312 (2010). doi:10.4028/www.scientific.net/MSF.638-642.3307
  35. Silva, E. P. Da *et al.* Isothermal transformations in advanced high strength steels below martensite start temperature. *Mater. Sci. Technol.* **31**, 808–816 (2015).
  36. Radcliffe, S. & Rollason, E. The kinetics of the formation of bainite in high-purity iron-carbon alloys. *J. Iron Steel Inst* **191**, 56–65 (1959).
  37. Oka, M. & Okamoto, H. Swing back in kinetics near Ms in hypereutectoid steels. *Met. Trans. A* **19**, 447–452 (1988).
  38. Jellinghaus, W. Anregung der Zwischenstufen-Umwandlung des Stahles durch kleine Mengen von  $\alpha$ -Eisen. *Arch. Eisenhütt* **23**, 459–470 (1952).
  39. Goodenow, R. ., Barkalow, R. . & Hehemann, R. . *Bainite transformations in hypoeutectoid steels.* Iron and Steel Institute, London (1969).
  40. Lange, H. & Mathieu, K. Ueber den Ablauf der Austenitumwandlung im unterkühlten Zustand bei Eisen-Nickel-Kohlenstoff-Legierungen. *KWI Eisenforsch* **20**, 125–134 (1938).
  41. Howard, R. . & Cohen, M. Austenite transformation above and within the martensite range. *Trans. AIME* **176**, 384–397 (1948).
  42. Babu, B. N. ., Bhat, M. ., Parker, E. . & Zacky, V. . A rapid magnetometric technique to plot isothermal transformation diagrams. *Met. Trans. A* **7**, 17–22 (1976).
  43. Ericsson, C. ., Bhat, M. ., Parker, E. . & Zackay, V. . Isothermal studies of bainitic and martensitic transformations in some low alloy steels. *Met. Trans. A* **7**, 1800–1803 (1976).
  44. Vettters, H., Dong, J., Bomas, H., Hoffmann, F. & Zoch, H. . Microstructure and fatigue strength of the roller-bearing steel 100Cr6 (SAE 52100) after two-step bainitisation and

- combined bainitic-martensitic heat treatment. *Int. J. Mater. Res.* **97**, 1432–1440 (2006).
45. Santofimia, M. J. *et al.* Microstructural development during the quenching and partitioning process in a newly designed low-carbon steel. *Acta Mater.* **59**, 6059–6068 (2011).
  46. Andrés, C. G. de, Caballero, F. G., Capdevila, C. & Álvarez, L. F. Application of dilatometric analysis to the study of solid–solid phase transformations in steels. *Mater. Charact.* **48**, 101 (2002).
  47. Kop, T. A. *A dilatometric study of the austenite/ferrite interface mobility.* (2000).
  48. Bohemen, S. M. C. Van. The nonlinear lattice expansion of iron alloys in the range 100 – 1600 K. *Scr. Mater.* **69**, 315–318 (2013).
  49. Bohemen, S. M. C. van. Austenite in multiphase microstructures quantified by analysis of thermal expansion. *Scr. Mater* **75**, 22–25 (2014).
  50. Koistinen, D. . & Marburger, R. . A general equation prescribing the extent of the austenite-martensite transformation in pure iron-carbon alloys and plain carbon steels. *Acta Met.* **7.1**, 59–60 (1959).
  51. Bohemen, S. M. C. van. Bainite and martensite start temperature calculated with exponential carbon dependence. *Mater. Sci. Technol* **28**, 487–495 (2012).
  52. Cullity, B. D. *Elements of x-ray diffraction.* (1956).
  53. Jatzcak, C. ., Larson, J. . & Shin, S. . Retained austenite and its measurements by X-ray diffraction. *Soc. Automot. Eng.* **453**, (1980).
  54. Goldstein, J. Scanning Electron Microscopy and X-Ray Microanalysis. *Springer* (2003).
  55. Goulas, C., Mecozzi, M. G. & Sietsma, J. Bainite Formation in Medium-Carbon Low-Silicon Spring Steels Accounting for Chemical Segregation. *Metall. Mater. Trans. A* **47**, 3077–3087 (2016).
  56. Caballero, F. ., Junceda, A. G., Capdevila, C. & Garcia de Andres, C. Evolution of Microstructural Banding during the Manufacturing Process of Dual Phase Steels. *Mater. Trans.* **47**, 2269–2276 (2006).
  57. Santofimia, M. J., Bohemen, S. M. C. Van & Sietsma, J. Combining bainite and martensite in steel microstructures for light weight applications. *J. South. African Inst. Min. Metall.* **113**, 143–148 (2013).
  58. Matsuda, H. & Bhadeshia, H. K. D. H. Kinetics of the Bainite Transformation. *Proc. R. Soc. Lond. A* **460**, 1707–1722 (2004).
  59. Parker, S. V. *Modelling of phase transformations in hot-rolled steels.* (1997).
  60. Chang, L. C. & Bhadeshia, H. K. D. H. Austenite films in bainitic microstructures. *Mater. Sci. Technol.* **11**, 874 (1995).
  61. Singh, S. B. & Bhadeshia, H. K. D. H. Estimation of bainite plate-thickness in low-alloy steels. *Mater. Sci. Eng., A* **245**, 72–79 (1998).
  62. Chang, L. . *Bainite Transformation and Novel Bainitic Rail Steels (PhD Thesis).* (1995).
  63. Guo, Y. *et al.* Effects of isothermal heat treatment on nanostructured bainite morphology and microstructures in laser clad coatings. *Appl. Surf. Sci.* **357**, 309–316 (2015).
  64. Lee, S., Lee, S. & Cooman, B. C. De. Reply to comments on ‘ Austenite stability of ultrafine-grained transformation-induced plasticity steel with Mn partitioning ’. *Scr. Mater.* **66**, 832–833 (2012).
  65. Wei, R. W., Wang, L. C., Xiao, Y. & Wang, L. Stability of Retained Austenite Through a Combined Intercritical Annealing and Quenching and Partitioning ( IAQP ) Treatment. *Acta Met.* **28**, 386–393 (2015).





# 7. Appendix

## 7.1. XRD calculation for all conditions

A detailed procedure for the XRD calculations is given in the following figures. The condition for which the calculation has been done is represented at the top left corner of the image. Both statistical and I/R error are given at the bottom of the image along with the calculated volume fraction of retained austenite.

63_A_30Cps_25apr17.raw #1								
model	Jatczak	EVA	CSE	Orientation Relations			MD correction	
Co Ka	0.179 nm			F{110}	F{110}	F{200}		
step size ° 2θ	0.035			A{111}	A{200}	A{220}		
step time (s)	2402							
hkl	R	obs max	I/R	$\sigma_{cse (I/R)}$	austenite fraction	austenite fraction	austenite fraction	I/R
			cps*2θ	cps*2θ	± cse	± cse	± cse	cps*2θ
ferrite								
F 110	49.4	51.925	0.3223	0.00102203				0.294
F 200	9.2	77.199	0.2785	0.00848951				
F 211	24.2	99.337	0.2818	0.00362446				
F 220	13.1	123.027	0.2975	0.00785803				0.286
austenite								
A 111	0.0	0.000	0.0000	0.00000000	0.000			0.000
A 200	19.0	59.529	0.0165	0.00095060	#DIV/0!	0.049		
A 220	14.8	89.869	0.0184	0.00191840		0.003	0.062	
A 311	25.7	111.150	0.0157	0.00172128			0.006	
results								
	without texture correction	orientation relations	with MD correction	averaging out texture				
	I/R	I/R	I/R	I/R				
average	0.29502		0.28967	0.29419				
$\sigma_{cse}$	0.00304	0.00304	0.00304	0.00310				
$\sigma_{I/R}$	0.02000		0.00546	0.02440				
average	0.01685		0.00000	0.01685				
$\sigma_{cse}$	0.00092	0.00092	0.00092	0.00092				
$\sigma_{I/R}$	0.00137	0.00000	0.00000	0.00000				
austenite %	5.4	3.7	0.0	5.4				
$\sigma_{cse}$ %	0.3	0.2	#DIV/0!	0.3				
$\sigma_{I/R}$ %	0.5	3.3	#DIV/0!	0.6				



63_A_ISO300_16may17.raw #1								
model	Jatczak	EVA	CSE	Orientation Relations			MD correction	
Co Ka	0.179 nm			F{110}	F{110}	F{200}		
step size ° 2θ	0.035			A{111}	A{200}	A{220}		
step time (s)	2402							
hkl	R	obs max	I/R	$\sigma_{cse}$ (I/R)	austenite	austenite	austenite	I/R
			cps*2θ	cps*2θ	fraction	fraction	fraction	cps*2θ
					± cse	± cse	± cse	
ferrite								
F 110	49.4	52.381	0.1696	0.00073642				0.158
F 200	9.2	77.198	0.1566	0.00414369				
F 211	24.2	99.695	0.1498	0.00212078				
F 220	13.1	123.904	0.1500	0.00332650				0.152
austenite								
A 111	0.0	0.000	0.0000	0.00000000	0.000			0.000
A 200	19.0	58.221	0.0039	0.00115689	#DIV/0!	0.023		
A 220	14.8	89.561	0.0003	0.00078134		0.007	0.002	
A 311	25.7	109.498	0.0017	0.00079151			0.005	
results	without texture correction	orientation relations	with MD correction	averaging out texture				
	I/R	I/R	I/R	I/R				
average	0.15652		0.15530	0.15869				
$\sigma_{cse}$	0.00144	0.00144	0.00144	0.00157				
$\sigma_{I/R}$	0.00929		0.00450	0.01007				
average	0.00197		0.00000	0.00197				
$\sigma_{cse}$	0.00053	0.00053	0.00053	0.00053				
$\sigma_{I/R}$	0.00183	0.00000	0.00000	0.00000				
austenite %	1.2	0.8	0.0	1.2				
$\sigma_{cse}$ %	0.3	0.2	#DIV/0!	0.3				
$\sigma_{I/R}$ %	1.1	1.3	#DIV/0!	1.1				

63_A_ISO260_aftercutting_polishing_09may17.raw #2								
model	Jatczak	EVA	CSE	Orientation Relations			MD correction	
Co Ka	0.179 nm			F{110}	F{110}	F{200}		
step size ° 2θ	0.035			A{111}	A{200}	A{220}		
step time (s)	2402							
hkl	R	obs max	I/R	$\sigma_{cse (I/R)}$	austenite	austenite	austenite	I/R
			cps*2θ	cps*2θ	fraction	fraction	fraction	cps*2θ
					± cse	± cse	± cse	
ferrite								
F 110	49.4	52.371	0.2302	0.00086051				0.213
F 200	9.2	77.226	0.2033	0.00552559				
F 211	24.2	99.712	0.2058	0.00378735				
F 220	13.1	123.889	0.2162	0.00479434				0.208
austenite								
A 111	0.0	0.000	0.0000	0.00000000	0.000			0.000
A 200	19.0	59.646	0.0054	0.00122077	#DIV/0!	0.023		
A 220	14.8	89.473	0.0044	0.00123906		0.005	0.021	
A 311	25.7	111.631	0.0047	0.00117106			0.006	
results	without texture correction	orientation relations	with MD correction	averaging out texture				
	I/R	I/R	I/R	I/R				
average	0.21386		0.21055	0.21307				
$\sigma_{cse}$	0.00207	0.00207	0.00207	0.00225				
$\sigma_{I/R}$	0.01222		0.00310	0.01485				
average	0.00486		0.00000	0.00486				
$\sigma_{cse}$	0.00070	0.00070	0.00070	0.00070				
$\sigma_{I/R}$	0.00050	0.00000	0.00000	0.00000				
austenite %	2.2	1.5	0.0	2.2				
$\sigma_{cse}$ %	0.3	0.2	#DIV/0!	0.3				
$\sigma_{I/R}$ %	0.3	1.3	#DIV/0!	0.3				

63_A_ISO245_16may17.raw #1								
model	Jatzcak	EVA	CSE		Orientation Relations			MD correction
Co Ka	0.179 nm				F{110}	F{110}	F{200}	
step size ° 2θ	0.035				A{111}	A{200}	A{220}	
step time (s)	2402							
hkl	R	obs max	I/R	$\sigma_{cse (I/R)}$	austenite	austenite	austenite	I/R
			cps*2θ	cps*2θ	fraction	fraction	fraction	cps*2θ
					± cse	± cse	± cse	
ferrite								
F 110	49.4	52.355	0.2348	0.00077248				0.204
F 200	9.2	77.170	0.1918	0.00542742				
F 211	24.2	99.676	0.1885	0.00261696				
F 220	13.1	123.862	0.2299	0.00559786				0.203
austenite								
A 111	0.0	0.000	0.0000	0.00000000	0.000			0.000
A 200	19.0	59.752	0.0085	0.00095199	#DIV/0!	0.035		
A 220	14.8	89.487	0.0097	0.00186091		0.004	0.048	
A 311	25.7	111.676	0.0105	0.00118266			0.009	
results	without texture correction	orientation relations	with MD correction	averaging out texture				
	I/R	I/R	I/R	I/R				
average	0.21122		0.20325	0.20500				
$\sigma_{cse}$	0.00207	0.00207	0.00207	0.00202				
$\sigma_{I/R}$	0.02449		0.00101	0.02584				
average	0.00957		0.00000	0.00957				
$\sigma_{cse}$	0.00080	0.00080	0.00080	0.00080				
$\sigma_{I/R}$	0.00098	0.00000	0.00000	0.00000				
austenite %	4.3	2.8	0.0	4.5				
$\sigma_{cse}$ %	0.3	0.2	#DIV/0!	0.4				
$\sigma_{I/R}$ %	0.6	2.5	#DIV/0!	0.7				

63_A_ISO240_16may17.raw #1								
model	Jatczak	EVA	CSE	Orientation Relations			MD correction	
Co Ka	0.179 nm			F{110}	F{110}	F{200}		
step size ° 2θ	0.035			A{111}	A{200}	A{220}		
step time (s)	2402							
hkl	R	obs max	I/R	$\sigma_{cse}$ (I/R)	austenite	austenite	austenite	I/R
			cps*2θ	cps*2θ	fraction	fraction	fraction	cps*2θ
					± cse	± cse	± cse	
ferrite								
F 110	49.4	52.296	0.2306	0.00094215				0.213
F 200	9.2	77.032	0.2074	0.00568955				
F 211	24.2	99.547	0.2029	0.00280498				
F 220	13.1	123.640	0.1986	0.00482762				0.203
austenite								
A 111	0.0	0.000	0.0000	0.00000000	0.000			0.000
A 200	19.0	59.501	0.0079	0.00145791	#DIV/0!	0.033		
A 220	14.8	89.665	0.0081	0.00171969		0.006	0.038	
A 311	25.7	111.415	0.0095	0.00186660			0.008	
results								
	without texture correction	orientation relations	with MD correction	averaging out texture				
	I/R	I/R	I/R	I/R				
average	0.20988		0.20813	0.21365				
$\sigma_{cse}$	0.00201	0.00201	0.00201	0.00214				
$\sigma_{I/R}$	0.01428		0.00733	0.01486				
average	0.00853		0.00000	0.00853				
$\sigma_{cse}$	0.00098	0.00098	0.00098	0.00098				
$\sigma_{I/R}$	0.00087	0.00000	0.00000	0.00000				
austenite %	3.9	2.4	0.0	3.8				
$\sigma_{cse}$ %	0.4	0.3	#DIV/0!	0.4				
$\sigma_{I/R}$ %	0.5	2.1	#DIV/0!	0.5				

63_A_ISO230_16may17.raw #1								
model	Jatczak	EVA	CSE	Orientation Relations			MD correction	
Co Ka	0.179 nm			F{110}	F{110}	F{200}		
step size ° 2θ	0.035			A{111}	A{200}	A{220}		
step time (s)	2402							
hkl	R	obs max	I/R	$\sigma_{cse}$ (I/R)	austenite	austenite	austenite	I/R
			cps*2θ	cps*2θ	fraction	fraction	fraction	cps*2θ
					± cse	± cse	± cse	
ferrite								
F 110	49.4	52.324	0.2260	0.00085055				0.200
F 200	9.2	77.116	0.1866	0.00548701				
F 211	24.2	99.609	0.1900	0.00277204				
F 220	13.1	123.742	0.1680	0.00389610				0.181
austenite								
A 111	0.0	0.000	0.0000	0.00000000	0.000			0.000
A 200	19.0	59.682	0.0161	0.00172718	#DIV/0!	0.067		
A 220	14.8	89.747	0.0113	0.00231646		0.007	0.057	
A 311	25.7	111.686	0.0117	0.00143171			0.011	
results	without texture correction	orientation relations	with MD correction	averaging out texture				
	I/R	I/R	I/R	I/R				
average	0.19265		0.19069	0.20088				
$\sigma_{cse}$	0.00183	0.00183	0.00183	0.00207				
$\sigma_{I/R}$	0.02427		0.01333	0.02184				
average	0.01303		0.00000	0.01303				
$\sigma_{cse}$	0.00107	0.00107	0.00107	0.00107				
$\sigma_{I/R}$	0.00270	0.00000	0.00000	0.00000				
austenite %	6.3	4.1	0.0	6.1				
$\sigma_{cse}$ %	0.5	0.3	#DIV/0!	0.5				
$\sigma_{I/R}$ %	1.4	3.6	#DIV/0!	1.3				

63_A_ISO220_15may17.raw #1								
model	Jatczak	EVA	CSE		Orientation Relations			MD correction
Co Ka	0.179 nm				F{110}	F{110}	F{200}	
step size ° 2θ	0.035				A{111}	A{200}	A{220}	
step time (s)	2402							
hkl	R	obs max	I/R	$\sigma_{cse (I/R)}$	austenite	austenite	austenite	I/R
			cps*2θ	cps*2θ	fraction	fraction	fraction	cps*2θ
					± cse	± cse	± cse	
ferrite								
F 110	49.4	52.273	0.2248	0.00104529				0.200
F 200	9.2	76.987	0.1886	0.00563774				
F 211	24.2	99.492	0.1891	0.00307995				
F 220	13.1	123.613	0.1889	0.00508534				0.189
austenite								
A 111	0.0	0.000	0.0000	0.00000000	0.000			0.000
A 200	19.0	59.654	0.0150	0.00187199	#DIV/0!	0.062		
A 220	14.8	89.697	0.0139	0.00241349		0.007	0.069	
A 311	25.7	111.315	0.0147	0.00202135			0.011	
results	without texture correction	orientation relations	with MD correction	averaging out texture				
	I/R	I/R	I/R	I/R				
average	0.19785		0.19450	0.20082				
$\sigma_{cse}$	0.00206	0.00206	0.00206	0.00217				
$\sigma_{I/R}$	0.01797		0.00796	0.02077				
average	0.01453		0.00000	0.01453				
$\sigma_{cse}$	0.00122	0.00122	0.00122	0.00122				
$\sigma_{I/R}$	0.00053	0.00000	0.00000	0.00000				
austenite %	6.8	4.4	0.0	6.7				
$\sigma_{cse}$ %	0.5	0.4	#DIV/0!	0.5				
$\sigma_{I/R}$ %	0.6	3.8	#DIV/0!	0.7				

63_A_ISO210_15may17.raw #1								
model	Jatzcak	EVA	CSE	Orientation Relations			MD correction	
Co Ka	0.179 nm			F{110}	F{110}	F{200}		
step size ° 2θ	0.035			A{111}	A{200}	A{220}		
step time (s)	2402							
hkl	R	obs max	I/R	$\sigma_{cse (I/R)}$	austenite	austenite	austenite	I/R
			cps*2θ	cps*2θ	fraction	fraction	fraction	cps*2θ
					± cse	± cse	± cse	
ferrite								
F 110	49.4	52.285	0.2297	0.00106156				0.193
F 200	9.2	77.076	0.1753	0.00585820				
F 211	24.2	99.539	0.1797	0.00265429				
F 220	13.1	123.629	0.1884	0.00502520				0.181
austenite								
A 111	0.0	0.000	0.0000	0.00000000	0.000			0.000
A 200	19.0	59.709	0.0177	0.00145649	#DIV/0!	0.072		
A 220	14.8	89.490	0.0160	0.00240690		0.005	0.084	
A 311	25.7	111.931	0.0201	0.00235790			0.012	
results								
	without texture correction	orientation relations	with MD correction	averaging out texture				
	I/R	I/R	I/R	I/R				
average	0.19329		0.18725	0.19491				
$\sigma_{cse}$	0.00206	0.00206	0.00206	0.00217				
$\sigma_{I/R}$	0.02490		0.00874	0.03023				
average	0.01796		0.00000	0.01796				
$\sigma_{cse}$	0.00122	0.00122	0.00122	0.00122				
$\sigma_{I/R}$	0.00204	0.00000	0.00000	0.00000				
austenite %	8.5	5.2	0.0	8.4				
$\sigma_{cse}$ %	0.5	0.3	#DIV/0!	0.5				
$\sigma_{I/R}$ %	1.3	4.5	#DIV/0!	1.5				



63_A_ISO200_10may17.raw #1								
model	Jatczak	EVA	CSE		Orientation Relations			MD correction
Co Ka	0.179 nm				F{110}	F{110}	F{200}	
step size ° 2θ	0.035				A{111}	A{200}	A{220}	
step time (s)	2402							
hkl	R	obs max	I/R	$\sigma_{cse (I/R)}$	austenite	austenite	austenite	I/R
			cps*2θ	cps*2θ	fraction	fraction	fraction	cps*2θ
					± cse	± cse	± cse	
ferrite								
F 110	49.4	52.271	0.2306	0.00096979				0.201
F 200	9.2	77.180	0.1876	0.00674217				
F 211	24.2	99.577	0.1871	0.00286382				
F 220	13.1	123.672	0.1525	0.00426009				0.175
austenite								
A 111	0.0	0.000	0.0000	0.00000000	0.000			0.000
A 200	19.0	59.721	0.0221	0.00180180	#DIV/0!	0.088		
A 220	14.8	89.654	0.0183	0.00166308		0.007	0.089	
A 311	25.7	111.549	0.0212	0.00240865			0.008	
results	without texture correction	orientation relations	with MD correction	averaging out texture				
	I/R	I/R	I/R	I/R				
average	0.18945		0.18786	0.20178				
$\sigma_{cse}$	0.00213	0.00213	0.00213	0.00246				
$\sigma_{I/R}$	0.03199		0.01829	0.02497				
average	0.02054		0.00000	0.02054				
$\sigma_{cse}$	0.00115	0.00115	0.00115	0.00115				
$\sigma_{I/R}$	0.00197	0.00000	0.00000	0.00000				
austenite %	9.8	5.9	0.0	9.2				
$\sigma_{cse}$ %	0.5	0.3	#DIV/0!	0.5				
$\sigma_{I/R}$ %	1.7	5.1	#DIV/0!	1.3				

## 7.2. Phase Fractions with Corresponding Errors

The errors calculated for the phases fractions are given in the Table 7.1. The error for the RA volume fraction is calculated from the XRD by summing up the I/R error and statistical error together. The error for the volume fraction of PM and FM are calculated based on the error of  $\pm 5$  °C with the dilatometry and thus the range of volume fractions for the temperature range of  $\pm 5$  °C is found to be the error for FM and PM. The error for the BF is calculated by adding the errors of PM, FM and RA since the volume fraction of BF is found by balancing the other three phases.

Table 7.1: Summary of the phase fractions for all conditions with error.

Isothermal Condition (°C)	PM Fraction	FM Fraction	RA Fraction	BF Fraction
300	-	$0.13 \pm 0.01$	$0.01 \pm 0.01$	$0.86 \pm 0.02$
260	-	$0.12 \pm 0.01$	$0.02 < \pm 0.01$	$0.85 \pm 0.01$
245 (M <sub>s</sub> )	-	$0.05 \pm 0.01$	$0.04 \pm 0.01$	$0.91 \pm 0.01$
240	$0.003 < \pm 0.001$	$0.03 \pm 0.01$	$0.04 \pm 0.01$	$0.93 \pm 0.01$
230	$0.026 \pm 0.005$	$0.16 \pm 0.01$	$0.06 \pm 0.01$	$0.75 \pm 0.03$
220	$0.070 \pm 0.009$	$0.05 \pm 0.01$	$0.07 \pm 0.01$	$0.81 \pm 0.01$
210	$0.139 \pm 0.013$	$0.32 \pm 0.02$	$0.09 \pm 0.02$	$0.45 \pm 0.04$
200	$0.214 \pm 0.016$	$0.38 \pm 0.02$	$0.10 \pm 0.02$	$0.31 \pm 0.05$

### 7.3. Vacuum Effect at the Start of the Isothermal Transformation

Figure 7.1 shows the effect of vacuum at the start of the isothermal treatment. When the vacuum is switched on at the beginning of the isothermal treatment (blue curve), a bump is observed at the point when the vacuum starts. But when the vacuum was not switched on at the start of the isothermal treatment, there was no bump observed in the dilatation curve (see orange curve). Thus the bump in curves seen in the Figure 3.18 (b) is due to the start of the vacuum at the beginning of the isothermal treatment.

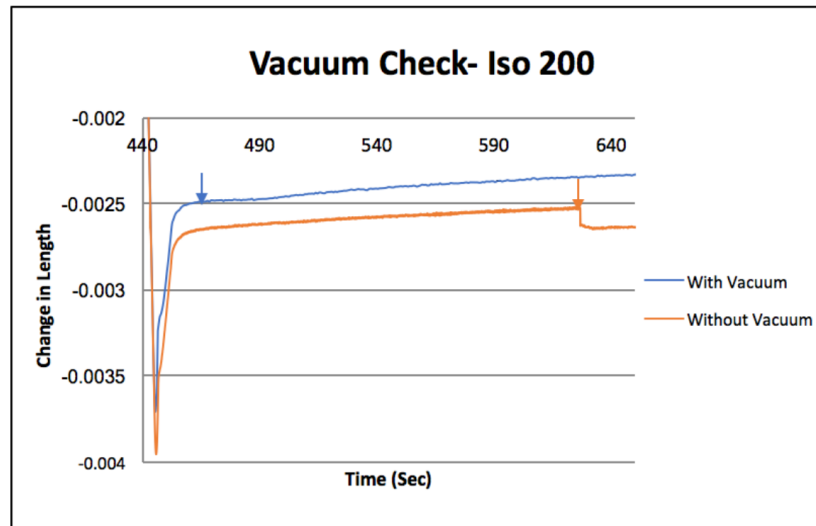


Figure 7.1: The effect of vacuum at the beginning of the transformation creating a bump in the dilatometry curves.